Simulation Strategies for Unusual EPR Spectra of Binuclear Mixed-Valence Manganese Complexes: Synthesis, Properties, and X-ray Structures of the $Mn^{II}Mn^{III}$ Complexes $[Mn_2(bpmp)(\mu\text{-}OAc)_2](ClO_4)_2\cdot H_2O$ and $[Mn_2(bcmp)(\mu\text{-}OAc)_2](ClO_4)_2\cdot CH_2Cl_2$

Habibe Diril,[1] Hsiu-Rong Chang,[2a] Mark J. Nilges,[2a] Xiaohua Zhang,[1] Joseph A. Potenza,*[,1] Harvey J. Schugar,*[,1] Stephan S. Isied,*[,1] and David N. Hendrickson*[,2b]

Contribution from the Department of Chemistry, D-006, University of California, San Diego, La Jolla, California 92093-0506, Department of Chemistry, Rutgers, The State University of New Jersey, New Brunswick, New Jersey 08903, and School of Chemical Sciences, University of Illinois, Urbana, Illinois 61801. *Received July 29, 1988*

Abstract: The preparation, single-crystal X-ray structures, variable-temperature magnetic susceptibility, and novel EPR data are presented for two mixed-valence $Mn^{II}Mn^{III}$ complexes. $[Mn_2(bpmp)(\mu\text{-}OAc)_2](ClO_4)_2\cdot H_2O$ (**1**), where $bpmp^-$ is the monoanion of 2,6-bis[bis(2-pyridylmethyl)aminomethyl]-4-methylphenol, crystallizes in the monoclinic space group $P2_1/n$ with a = 12.493 (1) Å, b = 21.583 (2) Å, c = 16.631 (2) Å, β = 95.31 (1)°, Z = 4; R_F = 0.061 and R_{wF} = 0.085 for 4298 unique reflections [$I > 3\sigma(I)$] at 297 (1) K. $[Mn_2(bcmp)(\mu\text{-}OAc)_2](ClO_4)_2\cdot CH_2Cl_2$ (**2**), where $bcmp^-$ is the monoanion of 2,6-bis(1,4,7-triazacyclonon-1-ylmethyl)-4-methylphenol, crystallizes in the orthorhombic space group $Pca2_1$, with a = 19.273 (1) Å, b = 15.155 (1) Å, c = 13.749 (3) Å, Z = 4; R_F = 0.074 and R_{wF} = 0.085 for 2324 unique reflections [$I > 3\sigma(I)$] at 296 (1) K. Trapped-valence $Mn^{II}Mn^{III}$ descriptions are appropriate for both **1** and **2**, where in each case the two Mn atoms are bridged by two bidentate acetate ions and by the phenoxide O atom of the $bpmp^-$ or $bcmp^-$ ligand. In the case of either **1** or **2** both Mn ions show pseudooctahedral coordination, and the Mn^{III} ion is Jahn–Teller distorted along the "z" direction. Two one-electron quasi-reversible cyclic voltammogram waves ($Mn^{II}Mn^{III} \rightarrow Mn^{II}_2$ and $Mn^{II}Mn^{III} \leftarrow Mn^{III}_2$, respectively) are seen for both **1** (+0.067 and +0.597 V vs Fc^+/Fc) and **2** (−0.133 and +0.347 V). Moderately well-resolved ^1H NMR signals are seen at room temperature for **1** in CD_2Cl_2 and **2** in CD_3CN. Magnetic susceptibility data are presented for polycrystalline samples of **1** in the 2.2–298 K range and **2** in the range 5–301.2 K. Fitting these data to the theoretical susceptibility equation for an isotropic exchange interaction ($H = -2JS_1\cdot S_2$) gave exchange parameters of −6.0 and −7.7 cm^{-1} for **1** and **2**, respectively. X-band EPR spectra for polycrystalline **1** and **2** in the 7.5–90 K range are illustrated and discussed. In addition to several other transitions the signals at $g \sim 4$ and $g \sim 2$ are associated with complexes in the $S = {}^3/_2$ excited and $S = {}^1/_2$ ground states, respectively. In a frozen glass (2:1:2 acetone/toluene/ethanol) at temperatures below ~15 K the X-band spectra of **1** and **2** exhibit a $g \sim 2$ signal structured with a 29-line manganese hyperfine pattern. It was necessary to run ~20 K Q-band EPR spectra of glasses of **1** and **2** to understand these hyperfine patterns. Through detailed computer simulation it was concluded that only the manganese hyperfine structure for the z component of the **g** tensor is resolved in the X- and Q-band spectra and that hyperfine structure for the g_x and g_y components is broad to the point of not contributing significantly to the observed EPR spectra. The absence of resolved structure from the g_x and g_y components is attributed to some combination of strain effects (i.e., distributions) associated with the g, A, or J values.

Two to four manganese ions serve as the active site for catalyzing the oxidation of two molecules of H_2O to give one molecule of O_2 in photosynthesis.[3] The Mn_x aggregate in photosystem II (PS II) cycles between five distinct oxidation levels labeled S_0, S_1, S_2, S_3, and S_4 according to the pioneering work of Joliot et al.[4] and Kok et al.[5] The S_n states contain manganese ions in various combinations of oxidation states, including Mn^{II}, Mn^{III}, and Mn^{IV}. These results have contributed to an increased interest in the structural, electronic, and solution properties of polynuclear manganese complexes.[6]

The oxygen-evolving complex in PS II exhibits an EPR signal with multiline manganese hyperfine structure in the S_2 state.[7a,8]

(1) Rutgers University.
(2) (a) University of Illinois. (b) University of California, San Diego. Address reprint requests to this address.
(3) (a) Renger, G. *Angew. Chem., Int. Ed. Engl.* **1987**, *26*, 643. (b) Dismukes, G. C. *Photochem. Photobiol.* **1986**, *43*, 99–115. (c) Govindjee; Kambara, T.; Coleman, W. *Photochem. Photobiol.* **1985**, *42*, 187–210. (d) Kambara, T.; Govindjee *Proc. Natl. Acad. Sci. U.S.A.* **1985**, *82*, 6119–6123. (e) Amesz, J. *Biochim. Biophys.* **1983**, *726*, 1–12. (f) Livorness, J.; Smith, T. D. *Struct. Bonding (Berlin)* **1982**, *48*, 2–44. (g) Sauer, K. *Acc. Chem. Res.* **1980**, *13*, 249–256. (h) Radmer, R.; Cheniae, G. In *Topics in Photosynthesis*; Barber, J., Ed.; Elsevier: Amsterdam, 1977. (i) Dismukes, G. C. *The Organization and Function of Manganese in the Water-Oxidizing Complex of Photosynthesis*; Academic: New York, 1986; Chapter 16, p 275.
(4) Joliot, P.; Barbieri, G.; Chaband, R. *Photochem. Photobiol.* **1969**, *10*, 302.
(5) Kok, B.; Forbush, B.; McGloin, M. P. *Photochem. Photobiol.* **1970**, *11*, 457.
(6) (a) Kirby, J. A.; Robertson, A. S.; Smith, J. P.; Thompson, A. C.; Cooper, S. R.; Klein, M. P. *J. Am. Chem. Soc.* **1981**, *103*, 5529–5537. (b) Nair, B. U.; Dismukes, G. C. *J. Am. Chem. Soc.* **1983**, *105*, 124–125. (c) Mathur, P.; Dismukes, G. C. *Ibid.* **1983**, *105*, 7093–7098. (d) Wieghardt, K.; Bossek, U.; Ventur, D.; Weiss, J. *J. Chem. Soc., Chem. Commun.* **1985**, 347–349. (e) Okawa, H.; Honda, A.; Nakamura, M.; Kida, S. *J. Chem. Soc., Dalton Trans.* **1985**, 59–64. (f) Mabad, B.; Cassoux, P.; Tuchagues, J. P.; Hendrickson, D. N. *Inorg. Chem.* **1986**, *25*, 1420–1431. (g) Pavacik, P. S.; Huffman, J. C.; Christou, G. *J. Chem. Soc., Chem. Commun.* **1986**, 43–44. (h) Lynch, M. W.; Hendrickson, D. N.; Fitzgerald, B. J.; Pierpont, C. G. *J. Am. Chem. Soc.* **1984**, *106*, 2041–2049. (i) Mabad, B.; Tuchagues, J. P.; Hwang, Y. T.; Hendrickson, D. N. *J. Am. Chem. Soc.* **1985**, *107*, 2801–2802. (j) Boucher, L. J.; Coe, C. G. *Inorg. Chem.* **1975**, *14*, 1289–1295. (k) Cooper, S. R.; Calvin, M. *J. Am. Chem. Soc.* **1977**, *99*, 6623. (l) Cooper, S. R.; Dismukes, G. C.; Klein, M. P.; Calvin, M. *Ibid.* **1978**, *100*, 7248. (m) Vincent, J. B.; Folting, K.; Huffman, J. C.; Christou, G. *Inorg. Chem.* **1986**, *25*, 996–999. (n) Sheats, J. E.; Czernuszewics, R. S.; Dismukes, G. C.; Rheingold, A. L.; Petrouleas, V.; Stubbe, J.; Armstrong, E. H.; Beer, R. H.; Lippard, S. J. *J. Am. Chem. Soc.* **1987**, *109*, 1435–1444. (o) Vincent, J. B.; Christou, G. *Inorg. Chim. Acta* **1987**, L41–L43. (p) Wieghardt, K.; Bossek, U.; Zsolnai, L.; Huttner, G.; Blondin, G.; Girerd, J. J.; Babonneau, F. *J. Chem. Soc., Chem. Commun.* **1987**, 651–653. (r) Vincent, J. B.; Christmas, C.; Huffman, J. C.; Christou, G.; Chang, H. R.; Hendrickson, D. N. *J. Chem. Soc., Chem. Commun.* **1987**, *236*–238.
(7) (a) Dismukes, G. C.; Siderer, Y. *Proc. Natl. Acad. Sci. U.S.A.* **1981**, *78*, 274–278. (b) Dismukes, G. C.; Ferris, K.; Watnick, P. *Photobiochem. Photobiophys.* **1982**, *3*, 243–256.

0002-7863/89/1511-5102$01.50/0

This signal has been attributed to either a binuclear $Mn^{III}Mn^{IV}$ site[7] or a tetranuclear $Mn^{III}_3Mn^{IV}$ site.[7b] The observation of this EPR signal has spawned a growing interest in characterizing mixed-valence multinuclear manganese complexes.

$Mn^{II}Mn^{III}$ binuclear complexes are rare.[9,10] Studies of these complexes are important for at least two reasons. To prepare models for the lower oxidation states S_0 and S_1, it is important to characterize the electronic structure and reactivities of the $Mn^{II}Mn^{III}$ complexes. Second, in recent communications[9-12] it has been shown that these $Mn^{II}Mn^{III}$ complexes exhibit EPR signals with well-resolved manganese hyperfine structure at low temperature. It is important to develop strategies to simulate these well-resolved hyperfine patterns to understand better the relatively broad, poorly resolved, difference EPR signal seen for the S_2 state. In this paper, the synthesis, structure, and physical properties (including a detailed analysis of the EPR hyperfine patterns) of the $Mn^{II}Mn^{III}$ complexes $[Mn_2(bpmp)(\mu\text{-}OAc)_2](ClO_4)_2\cdot H_2O$ (**1**) and $[Mn_2(bcmp)(\mu\text{-}OAc)_2](ClO_4)_2\cdot CH_2Cl_2$ (**2**) are presented. The ligands $bpmp^-$ and $bcmp^-$ have the following structures:

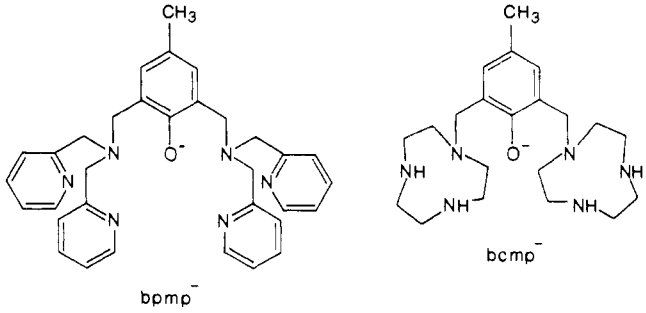

Experimental Section

1. Preparation of Ligands. Reagent grade chemicals were used as supplied. Bis(2-pyridylmethyl)amine was purchased from Nepera Chemicals and 2,6-bis(chloromethyl)-4-methylphenol was obtained from Trans World Chemicals and stored at −20 °C. The resins SP-Sephadex C-25 (Pharmacia) and Prep-Pak 500-C_{18} packing (Waters, 37–50 μm) were used for ion exchange and preparative reverse-phase silica gel chromatographic separations, respectively. The C_{18} resin was packed in ~80% MeOH–20% H_2O, washed with decreasing concentrations of MeOH, water, and then 0.05 M HCl before use. The column was cleaned with 65% CH_3CN–35% (0.05 M) TFA followed by H_2O until the pH of the effluent was 7. Elemental analyses were performed by Robertson Laboratory Inc., Madison, NJ.

2,6-Bis[bis(2-pyridylmethyl)aminomethyl]-4-methylphenol (bpmp). This ligand was synthesized using the method of Suzuki et al.[13]

2,6-Bis(1,4,7-triazacyclonon-1-ylmethyl)-4-methylphenol hexahydrochloride (bcmp·6HCl) was prepared by two different methods as follows. One is described below and the other is given in ref 14.

1,4,7-Tris(*p*-tolylsulfonyl)-1,4,7-triazacyclononane. This compound was prepared following the procedure of Wieghardt et al.[15]

1,4,7-Triazacyclononane Trihydrochloride. 1,4,7-Tri(*p*-tolylsulfonyl)-1,4,7-triazacyclononane (11.00 g, 18.6 mmol) was dissolved in 53 mL of concentrated H_2SO_4 and purged with N_2 gas. The resulting yellow solution was heated with stirring to 120–130 °C for 6 h. The solution was cooled in ice and slowly added to 450 mL of cold absolute ethanol. The mixture was then added to 450 mL of cold anhydrous ether, and the precipitate was collected by filtration, dissolved in a minimum volume of water, and filtered through a fine fritted funnel. The filtrate was made basic (pH ~ 12) with 12 M NaOH and extracted with small portions of chloroform. The chloroform layer was dried over anhydrous $MgSO_4$ and filtered. The yellowish wax obtained after concentrating the chloroform layer by rotary evaporation was dissolved in 25 mL of a 30:70 mixture of absolute ethanol and ether. Addition of 5 mL of concentrated HCl and cooling gave a white precipitate, which was washed with absolute ethanol and ether and then vacuum dried; yield 3.56 g, 80%.

bcmp·6HCl·2H₂O. 1,4,7-Triazacyclononane trihydrochloride (100 mg, 0.419 mmol) was dissolved in 50 mL of methanol by adding triethylamine (174 μL, 1.25 mmol). 2,6-Bis(chloromethyl)-4-methylphenol (43 mg, 0.21 mmol) was added slowly with stirring. More triethylamine (174 μL, 1.25 mmol) was added to raise the pH to ~8.5. The reaction mixture was stirred for 20 h. After the solvent was evaporated under reduced pressure, the residue was dissolved in a minimum amount of water, and 2 M NaOH was added to make it basic (pH 12). After triethylamine was evaporated under reduced pressure, the residue was dissolved in a minimum volume of water, acidified with 6 M HCl, and concentrated to dryness by rotary evaporation. The crude product bcmp·6HCl was purified twice by C-18 column chromatography. The white precipitate was chromatographed on SP Sephadex C-25 (Na^+ form). The column was washed with copious amounts of H_2O, followed by one column volume of each of 0.05, 0.1, 1, and 3 M HCl. The effluent was monitored at 280 nm. A band that eluted with 3–4 M HCl was collected and concentrated to dryness by rotary evaporation. The residue was further purified by preparative C-18 column chromatography (1.5 × 18 cm) while the effluent was monitored at 280 nm. The sample was dissolved in a minimum volume of 0.05 M HCl and applied to the resin. The first band (λ_{max} = 282 nm) was eluted slowly (1.2 mL/min) with 0.05 M HCl from the column and concentrated to dryness by rotary evaporation to give 1.3 g (49% yield) of white solid. The ligand was further purified by rechromatography on a C-18 column with 0.05 M HCl. Note: A number of unidentified bands that elute directly after bcmp·6HCl also have λ_{max} at 282 nm with additional shoulders at 270–276 nm. A yield of 36.3 mg (28% yield) of bcmp·6HCl·2H_2O was obtained. Anal. Calcd for $C_{21}H_{38}N_6\cdot 6HCl\cdot 2H_2O$: C, 39.14; H, 7.35; N, 13.04. Found: C, 38.94; H, 7.69; N, 12.86. ^1H NMR (D_2O, 400 MHz) 2.1 (s, 3 H, CH_3), 2.89 (t, 8 H, CH_2), 3.08 (t, 8 H, CH_2), 3.48 (s, 8 H, CH_2), 3.78 (s, 4 H, CH_2), 7.08 (s, 2 H, ArH).

2. Preparation and Crystallization of Manganese Complexes. Manganese trifluoromethanesulfonate ($Mn(TFMS)_2$) was prepared by following a procedure reported for cupric triflate.[16] TFMS (7.3 mL) was added to a slurry of $MnCO_3$ (4.6 g, 0.04 mol) in 200 mL of CH_3CN. The mixture was stirred and heated at 55–60 °C for 15 min. The insoluble brown material was filtered through a fine-fritted funnel while hot. The yellowish filtrate was concentrated to a white waxy solid by rotary evaporation. The residue was washed with anhydrous ether to yield a white solid, which was dried under vacuum over drierite ($CaSO_4$); yield 10.0 g, 64%.

$[Mn_2(bpmp)(\mu\text{-}OAc)_2](ClO_4)_2$. Method 1. To 0.50 g (0.94 mmol) of ligand bpmp in 8.5 mL of 85% ethanol, 0.25 g (0.94 mmol) of $Mn(OAc)_3\cdot 2H_2O$ and 0.51 g (3.75 mmol) of NaOAc were added. The reaction mixture was stirred for 15 min, and the pH of the turbid, dark-brown reaction mixture was adjusted to 2.6 with a few drops of concentrated $HClO_4$. A dark green color developed upon acidification. To precipitate the product, $NaClO_4$ (0.83 g) was added to the reaction mixture which was stored at ~8 °C for 5 days. The blackish-gray precipitate that formed from the dark-green solution was collected on a fritted funnel and washed with small volumes of ethanol, 2-propanol, and absolute ether consecutively. The precipitate was dried in a desiccator under vacuum. The yield of the crude product was 0.17 g (37%) of $[Mn_2(bpmp)(\mu\text{-}OAc)_2](ClO_4)_2$.

The crude product was dissolved in a nearly saturated solution of $NaClO_4$ in CH_3CN and diluted with petroleum ether. Slow evaporation of this mixture in air resulted in large dark-green crystals of $[Mn_2(bpmp)(\mu\text{-}OAc)_2](ClO_4)_2\cdot H_2O$ suitable for diffraction studies. Since no special precautions were taken to dry the solvents rigorously or to exclude atmospheric moisture, the presence of lattice water is not surprising. Anal. Calcd for $C_{37}H_{39}N_6Cl_2O_{13}Mn_2\cdot H_2O$: C, 45.60; H, 4.24; N, 8.62; Cl, 7.27; Mn, 11.27. Found: C, 45.38; H, 4.24; N, 8.47; Cl, 7.36; Mn, 10.6 (determined by ICP).

$[Mn_2(bpmp)(\mu\text{-}OAc\text{-}d_3)_2](ClO_4)_2$. The ligand bpmp (0.25 g, 4.71×10^{-4} mol) was dissolved in 2.25 mL of an ethanol:D_2O (85:15 v/v) mixture and purged with argon for 15 min. A deaerated solution of $Mn(TFMS)_2$ (0.184 g, 4.71×10^{-4} mol) in 2 mL of the ethanol:D_2O mixture was transferred to the ligand solution via a gas-tight syringe and left

(8) Hansson, O.; Andreasson, L. E. *Biochim. Biophys. Acta* **1982**, *679*, 261–268.
(9) Suzuki, M.; Mikuriya, M.; Murata, S.; Vehara, A.; Oshio, H.; Kida, S.; Saito, K. *Bull. Chem. Soc. Jpn.* **1987**, *60*, 4305–4312.
(10) (a) Buchanan, R. M.; Oberhausen, K. J.; Richardson, J. F. *Inorg. Chem.* **1988**, *27*, 971–973. (b) Dismukes, G. C.; Sheats, J. E.; Smegal, J. A. *J. Am. Chem. Soc.* **1987**, *109*, 7202–7203.
(11) Diril, H.; Chang, H.-R.; Zhang, X.; Larsen, S. K.; Potenza, J. A.; Pierpont, C. G.; Schugar, H. J.; Isied, S. S.; Hendrickson, D. N. *J. Am. Chem. Soc.* **1987**, *109*, 6207–6208.
(12) Chang, H.-R.; Diril, H.; Nilges, M. J.; Zhang, X.; Potenza, J. A.; Schugar, H. J.; Hendrickson, D. N.; Isied, S. S. *J. Am. Chem. Soc.* **1988**, *110*, 625–627.
(13) Suzuki, M.; Kanatomi, J.; Murase, I. *Chem. Lett., Chem. Soc. Jpn.* **1981**, 1745–1748.
(14) Diril, H. Ph.D. Thesis, 1988, Rutgers, The State University of New Jersey.
(15) Wieghardt, K.; Nuber, B.; Weiss, J. *Chem. Ber.* **1979**, *112*, 2220–2230.
(16) (a) Jenkins, C. L.; Kochi, J. K. *J. Am. Chem. Soc.* **1972**, *94*, 843. (b) A reviewer pointed out a preparation of $Mn(TFMS)_2$: Bryan, P. S.; Dabrowiak, J. C. *Inorg. Chem.* **1975**, *14*, 296–299.

stirring under argon for 1 h. After addition of 0.26 g of NaOAc-d_3 the uncorrected pH was adjusted to 2.97 with 25% $HClO_4$ in ethanol:D_2O mixture, and 0.84 g of $NaClO_4$ was added. The solution was stirred in air for 1.5 h and then stored at 8 °C for 2 days.

The green precipitate that formed along with white salts was collected by filtration and washed with 2-propanol and ether. Crystallization was achieved by diffusion of petroleum ether into a $NaClO_4$-saturated CH_3CN solution of the crude product at ~8 °C for 4 days, followed by slow evaporation of the solvent at room temperature.

$[Mn_2(bcmp)(\mu\text{-}OAc)_2](ClO_4)_2$. The ligand bcmp·6HCl was dissolved in a minimum amount of H_2O, and the solution was made basic with 2 N NaOH. Free bcmp was extracted into $CHCl_3$. The $CHCl_3$ layer was dried over anhydrous $MgSO_4$ and concentrated by rotary evaporation to yield an oily residue (50 mg, 0.13 mmol), which was dissolved in 2.5 mL of absolute ethanol. The solution was stirred for 30 min under argon saturated with ethanol. To this solution, $Mn(OAc)_2·4H_2O$ (43 mg, 1.75 mmol) was added, and it was stirred for 45 min under argon, after which $Li(OAc)·2H_2O$ (54.4 mg, 0.53 mmol) and $NaClO_4$ (116.2 mg, 0.95 mmol) were dissolved in the solution.

Exposure of the solution to dry air resulted in a dark green solution and within 5 h a dark-green precipitate formed. The percipitate was collected on a fine-fritted funnel and washed with ether and a few drops of absolute ethanol:ether (35:65) mixture (~4 mL total volume). The precipitate was washed with ether again and dried in the desiccator under vacuum; yield 64 mg, 89% $[Mn_2(bcmp)(\mu\text{-}OAc)_2](ClO_4)_2$. Anal. Calcd for $C_{25}H_{43}N_6Cl_2O_{13}Mn_2$: C, 36.78; H, 5.31; N, 10.29; Cl, 8.68; Mn, 13.46. Found: C, 36.95; H, 5.13; N, 10.04; Cl, 8.92; Mn, 13.17 (determined by ICP).

Crystallization was achieved as follows: The dark-green precipitate was dissolved in warm methylene chloride and filtered while hot, and the filtrate was concentrated by slow evaporation of the solvent at 40 °C and then filtered again. Dark needlelike crystals of $[Mn_2(bcmp)(\mu\text{-}OAc)_2](ClO_4)_2·CH_2Cl_2$ deposited during slow evaporation of the CH_2Cl_2 through a pinhole into a closed beaker containing drierite.

$[Mn_2(bcmp)(\mu\text{-}OAc\text{-}d_3)_2](ClO_4)_2$. Free bcmp (26 mg, 6.7×10^{-5} mol) was dissolved in 0.7 mL of absolute ethanol and purged with argon for 20 min. A degassed solution of $Mn(TFMS)_2$ (34 mg, 8.7×10^{-5} mol) in 0.9 mL of absolute ethanol was added to the ligand solution with a gas-tight syringe, and the reaction mixture was stirred under argon for 45 min. After addition of NaOAc-d_3 (38 mg, 4.5×10^{-4} mol) and $NaClO_4$ (60 mg, 4.9×10^{-4} mol), the reaction mixture was stirred for an additional 5 min under argon before exposing to air. Isolation of the deuterated compound was achieved by following the earlier procedure.

CAUTION: Perchlorate salts are explosive, and care should be exercised in handling these compounds even though we experienced no problems.

3. X-ray Diffraction Studies. A dark-green single crystal of **1** of dimensions 0.2 × 0.45 × 0.55 mm was cleaved from a large six-sided plate and mounted on the end of a glass fiber. A dark-green crystal of **2** of dimensions 0.25 × 0.48 × 0.1 mm was mounted inside a glass capillary and prevented from desolvating by a small amount of mother liquor well removed from the crystal. All diffraction measurements were made with an Enraf-Nonius CAD-4 diffractometer. The Enraf-Nonius structure determination package[17] was used for data collection, data processing, and structure solution. Crystal data and additional details of the data collection and refinement are given in Table I. Intensity data were collected and corrected for decay, absorption (empirical, ψ scan), and *Lp* effects. For **2**, systematic extinctions indicated the space group to be either $Pca2_1$ or *Pbcm*; successful solution and refinement of the structure confirmed the noncentrosymmetric choice $Pca2_1$.

The structures were solved by direct methods[18] and refined on *F* by using full-matrix least-squares techniques. For complex **1**, an initial *E* map revealed coordinates for both unique Mn atoms and part of the ligand. The remaining non-hydrogen ligand atoms were located on successive difference Fourier maps. The methyl C atom C(37) showed a relatively high temperature factor as did the perchlorate O atoms and the lattice water molecule O(W). Indeed, the temperature factor of the water molecule is sufficiently high (B = 38 (1) Å^2) to suggest that this site may be either disordered or partially occupied. The benzoate homologue of **1**,[9] $[Mn_2(bpmp)(\mu\text{-}OBz)_2](ClO_4)_2·H_2O$, was found to have one disordered lattice water molecule per complex equally distributed over two lattice sites. These workers also reported the preparation of **1** as a monohydrate. Finally, we note that removal of water from the structure of **1** resulted in a significant increase in the observed *R* factor. One perchlorate group was disordered and was modeled by assuming six partially occupied sites for three of the O atoms. Except for the methyl and water groups for which H atoms were not located, H atoms were added to the model at calculated positions with temperature factors set equal to $B_H = 1.3B_N$, where N is the atom bonded to H. H atom coordinates were refined isotropically. Several cycles of refinement with all ligand atoms anisotropic and with ClO_4^- oxygen atoms isotropic led to convergence with R_F = 0.061, R_{wF} = 0.085, and goodness of fit (GOF) = 2.82. The highest seven peaks in the final difference map (0.46–0.77 e$^-$/Å^3) were located 1.30–1.60 from the perchlorate Cl atoms. Final atomic coordinates for **1** are given in the supplementary material (see paragraph at the end of the paper).

For complex **2**, an *E* map based on 339 phases from the starting set with the highest combined figure of merit revealed both Mn atoms and several atoms in the coordination sphere. The remaining ligand atoms and the perchlorate atoms were located on successive difference maps. Location of the CH_2Cl_2 solvate molecule proved difficult. Following refinement of the cation and perchlorate anions, a difference map was prepared. The highest 10 peaks (0.71–1.87 e$^-$/Å^3) were located near each other in a cavity in the structure and were not residuals of known atoms. Geometric considerations suggested that they arose from severely disordered CH_2Cl_2 solvent atoms. Mass spectral analysis confirmed the presence of CH_2Cl_2 in the crystals. All attempts to model this disorder were inadequate to some extent; the best fit to the e$^-$ density was obtained by assuming two sites for the C atom and three sites for each Cl atom. Several ligand H atoms were located on a difference map, and the remaining ones were added at calculated positions. CH_2Cl_2 hydrogen atoms were not added to the model. Hydrogen atom temperature factors were set as for **1**; H atom parameters were not refined. Several cycles of refinement reduced R_F, R_{wF}, and GOF to 0.074, 0.085, and 2.50, respectively. The five largest peaks on a final difference map (0.52–0.60 e$^-$/Å^3) were located 1.10–1.61 Å from the three chlorine atoms Cl(1)–Cl(3). Final atomic coordinates are tabulated in the supplementary material. Lists of anisotropic thermal parameters, H atom parameters, and calculated and observed structure factors for both structures are given in the supplementary material.

Table I. Crystal and Refinement Data for **1** and **2**

	1	**2**
fw	956.6	901.4
a, Å	12.493 (1)	19.273 (2)
b, Å	21.583 (2)	15.155 (1)
c, Å	16.631 (2)	13.749 (3)
β, deg	95.31 (1)	90
V, Å^3	4465	4016
space group	$P2_1/n$	$Pca2_1$
Z	4	4
no. refs used to det'n cell const	25	25
d_{calcd}, g/cm^3	1.423	1.503
d_{obsd}, g/cm^3	1.44 (1)	1.54 (1)
rad used	graph mono Mo Kα (0.710 73 Å)	
linear abs coeff, cm^{-1}	7.25	9.33
cryst dimens, mm	0.2 × 0.45 × 0.55	0.25 × 0.48 × 0.1
rel trans factor range	0.96–1.00	0.94–1.00
diffractometer	Enraf-Nonius CAD-4	
data coll method	θ–2θ	
2θ range deg	$4 < 2\theta < 45$	
temp, K	297 (1)	296 (1)
scan range, deg	0.75 + 0.30 tan θ	0.60 + 0.30 tan θ
weighting scheme[a]	$w = 4(F_o)^2/[\sigma(F_o)^2]^2$	
std reflcns, %	0.9	0.8
no. unique data coll	6458	2973
no. data used in refinement	4298	2324
data:parameter ratio	7.08	5.48
final GOF	2.82	2.50
final R_F, R_{wF}	0.061, 0.085	0.0748, 0.085
final largest shift/esd	0.7[b]	0.1[b]
highest peak in final diff map, e/Å^3	0.77	0.60

[a] $[\sigma(F_o)^2]^2 = [S^2(C + R^2B) + (pF_o^2)^2]/(Lp)^2$, where S is the scan rate, C is the integrated peak count, R is the ratio of scan to background counting time, B is the total background count, and p is a factor used to down-weight intense reflections. For these structures, p = 0.04. [b] Largest shift/esd for heavy atoms of the cations. The largest shift/esd for compound **1** were observed for a H atom (1.09) and for a disordered O(ClO_4) atom (1.13). The largest shift/esd for compound **2** was observed for a disordered methylene chloride C atom (0.95).

(17) Enraf-Nonius structure determination package, Enraf-Nonius, Delft, Holland, 1983.

(18) Main, P.; Fiske, S. J.; Hull, S. E.; Lessinger, L.; Germain, G.; Declercq, J.-P.; Woolfson, M. M. MULTAN 82. A System of Computer Programs for the Automatic Solution of Crystal Structures from X-ray Diffraction Data. Universities of York, England and Louvain, Belgium, 1982.

Scheme I

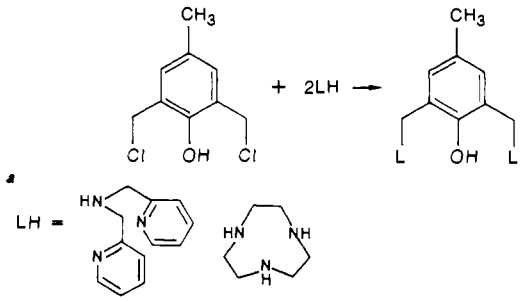

4. Electrochemistry. Differential pulse polarography and cyclic voltammetry were performed with a Princeton Applied Research Model 174A polarographic analyzer and a Model 173 potentiostat. Measurements were done in CH_3CN using a $Ag/AgNO_3$ (0.1 M $AgNO_3$ in CH_3CN) reference electrode, a platinum disk working electrode, and a Pt wire auxiliary electrode. Manganese complexes ($\sim 1.0 \times 10^{-3}$ M) were dissolved in 0.1 M $(n\text{-}Bu)_4NClO_4$ CH_3CN solutions. Ferrocene was used as an external standard[19] ($E_{1/2}$ = 0.075 V vs $Ag/AgNO_3$).

5. UV-Visible Spectra. UV-visible spectra were recorded on either an IBM 9430, a Hewlett-Packard 8450A diode array, or a Cary 118 spectrophotometer. Solid-state UV-visible spectra were recorded on transparent methyl acrylate Degalan V26 (Fluka Co.) films that were obtained by evaporation of the solvent from a slurry prepared by stirring the methyl acrylate with CH_3CN or CH_2Cl_2 under nitrogen and pouring it onto a glass plate. Near-IR spectra from 1500 to 800 nm were recorded on an Aviv 14DS UV-visible spectrophotometer interfaced with an AT&T computer.

6. Nuclear Magnetic Resonance Spectroscopy. ^1H NMR spectra were recorded on a Varian XL 400 spectrometer.

7. Electron Paramagnetic Resonance Spectroscopy. X-band EPR spectra were recorded with a Bruker ER-220D spectrometer operating at 9.5 GHZ equipped with an Air Products positive helium cooling temperature controller above 7.5 K (Illinois ESR Research center at the University of Illinois). Q-band EPR spectra were run with a Varian E-9 spectrometer operating at 35 GHz with temperature available down to $\sim$20 K (National Biomedical ESR center at the University of Wisconsin at Milwaukee). For measurements at X-band, the magnetic field was calibrated with a Varian E-500 NMR Gauss meter, and the frequency measured with an EIP 548A frequency meter.

Simulated EPR spectra were generated by means of the program MPOW2 running on an IBM-AT computer connected to an IBM digital plotter. Program MPOW2 was modified from the powder simulation program POW.[20] In this program, the transition frequencies for a spin $S = {}^1/_2$ system are calculated by using a spin Hamiltonian and perturbation theory correct through second order in the hyperfine interaction.

The method of Guilbault and Lubrano[21] was used to calculate the concentration of Mn^{2+} in aqueous solutions.

8. Magnetic Susceptibility Measurements. Variable-temperature, solid-state magnetic susceptibility data were measured by using a series 800 VTS-50 SQUID susceptometer (S.H.E. Corp.). The susceptometer was operated at a magnetic field strength of 10 kG. Diamagnetic corrections were estimated from Pascal's constants and subtracted from the experimental susceptibility data to obtain molar paramagnetic susceptibilities. These susceptibilities were fit to the appropriate theoretical expressions by means of a least-squares-fitting computer program.[22]

Results and Discussion

Synthesis of Compounds. The ligands bpmp[13] and bcmp were synthesized following Scheme I. The manganese complexes $[Mn_2(bpmp)(\mu\text{-}OAc)_2](ClO_4)_2\cdot H_2O$ (**1**) and $[Mn_2(bcmp)(\mu\text{-}OAc)_2](ClO_4)_2\cdot CH_2Cl_2$ (**2**) were obtained as perchlorate salts from the reaction of manganese(II) salts and either the bpmp or the bcmp ligand in the presence of sodium or lithium acetate.

Electrochemistry. Two quasi-reversible cyclic voltammetric waves are observed for **1** at potentials of $E_{1/2}$ = 0.067 and 0.597 V vs Fc^+/Fc (figure in supplementary material). These waves correspond to the processes $Mn^{II}Mn^{III} \rightarrow Mn_2^{II}$ and $Mn^{III}Mn^{II} \rightarrow Mn_2^{III}$, respectively. For complex **2** these two waves occur at -0.133 and +0.347 V. The instability of the $Mn^{III}Mn^{III}$ state is more pronounced for the $bpmp^-$ ligand than the $bcmp^-$ ligand. This can be shown by holding the potential at the oxidation wave of the $Mn^{III}Mn^{III}$ for a given time and measuring the peak height upon reduction to the $Mn^{II}Mn^{III}$ complex.

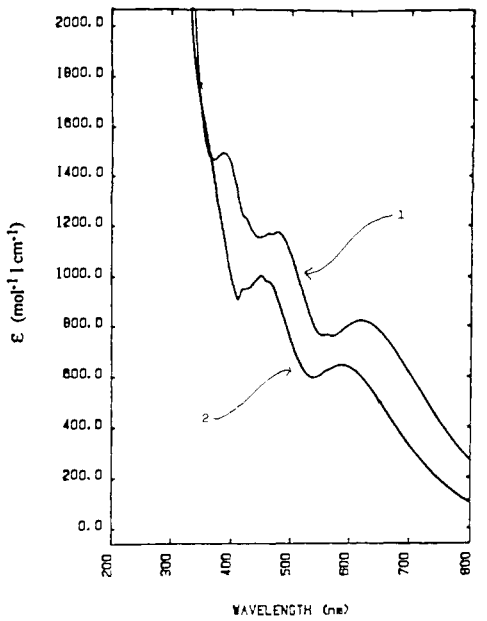

Figure 1. Room-temperature UV-visible electronic absorption spectra of $[Mn_2(bpmp)(\mu\text{-}OAc)_2](ClO_4)_2\cdot H_2O$ (**1**) and $[Mn_2(bcmp)(\mu\text{-}OAc)_2](ClO_4)_2\cdot CH_2Cl_2$ (**2**) in CH_3CN.

UV-Visible Electronic Absorption. The UV-visible spectra of **1** and **2** in acetonitrile at room temperature are presented in Figure 1. Since the spectra of these complexes dispersed in mineral oil mulls are similar to the solution spectra, the molecular structures of the crystalline complexes appear to be closely conserved in acetonitrile solutions. The spectra of **1** and **2** dispersed in Degalan films at 80 K exhibit slightly better resolution than the room-temperature CH_3CN solutions with the absorption of **2** at $\sim$360 nm (shoulder in Figure 1) better defined; also, the similarity of the spectra of **1** and **2** is more obvious with samples dispersed in Degalan films. Essentially identical solution spectra recently have been reported by other workers for complex **1** and its homologue containing bridging benzoate groups.[9]

Since the binuclear Mn^{II}_2 complexes resulting from the one-electron reduction of **1** and **2** essentially are spectroscopically transparent at wavelengths longer than 400 nm, the prominent ($\epsilon > 600$ per dimer) electronic absorptions of the two mixed-valence $Mn^{II}Mn^{III}$ complexes shown in Figure 1 originate from the Mn^{III} subunits. On the basis of spectra reported for various Mn^{III} mononuclear and binuclear complexes, it is possible to suggest approximate assignments for some of the features in Figure 1. Since a binuclear Mn^{III}_2 complex with two phenoxo bridges[6m] exhibits a prominent absorption at 323 nm (ϵ = 8400 per dimer or 2100 per Mn^{III} phenoxo bond) presumably from charge transfer, the somewhat less intense absorptions of complexes **1** and **2** at approximately 360-400 nm may be assigned to phenoxo-Mn^{III} LMCT. The other absorptions of the binuclear phenoxo Mn^{III} complex at 522 nm (ϵ = 215) and 424 nm (ϵ = 336) are thought to be LF absorptions. Presumably analogous LF absorptions with comparable energies and intensities are exhibited by monomeric Mn^{III} complexes such as the tris(picolinate) [518 nm (ϵ = 518), 424 nm (ϵ = 380)].[23] On this basis, the absorptions of **1** and **2** at approximately 590-630 nm and 450-480 nm may reasonably be assigned as LF bands. Numerous spin-forbidden electronic transitions in this energy region are predicted for six-coordinate Mn^{III} ions.[24] The "structure" on the LF absorption may arise

(19) Gagne, R. R.; Koval, C. A.; Lisensky, G. C. *Inorg. Chem.* **1980**, *19*, 2854-2855.

(20) Belford, R. L.; Nilges, M. J. Computer Simulation of EPR Powder Spectra. Symposium on Electron Paramagnetic Resonance Spectroscopy, Rocky Mountain Conference on Analytical Chemistry, Denver, Aug 1979.

(21) Guilbault, G. C.; Lubrano, G. J. *Anal. Lett.* **1968**, *1*, 725-733.

(22) Chandler, J. P. Program 66 of the Quantum Chemistry Program Exchange, Indiana University, Bloomington, IN.

(23) Yamaguchi, K.; Sawyer, D. T. *Inorg. Chem.* **1985**, *24*, 971-976.

Table II. Selected Bond Distances in Angstroms for **1** and **2** (Values for **2** Are Listed below Those for **1**[a]

Mn(1)	Mn(2)	3.447 (1)	N(5)	C(17)	1.343 (8)
		3.422 (3)			1.45 (2)
Mn(1)	O(2)	2.166 (4)	N(6)	C(18)	1.514 (8)
		2.135 (9)			1.54 (2)
Mn(1)	O(4)	2.066 (5)	N(6)	C(19)	1.490 (9)
		2.09 (1)			1.47 (2)
Mn(1)	O(5)	2.193 (4)	N(6)	C(26)	1.509 (8)
		2.17 (1)			1.47 (2)
Mn(1)	N(1)	2.271 (6)	C(5)	C(6)	1.51 (1)
		2.26 (1)			1.55 (2)
Mn(1)	N(2)	2.210 (6)	C(7)	C(8)	1.479 (9)
		2.22 (1)			1.46 (2)
Mn(1)	N(3)	2.324 (5)	C(17)	C(18)	1.49 (1)
		2.23 (1)			1.49 (2)
Mn(2)	O(1)	1.927 (5)	C(19)	C(20)	1.46 (1)
		2.01 (1)			1.51 (3)
Mn(2)	O(3)	2.090 (4)	C(25)	C(31)	1.492 (9)
		2.056 (9)			1.51 (2)
Mn(2)	O(5)	1.903 (4)	C(26)	C(27)	1.50 (2)
		1.957 (9)			1.51 (2)
Mn(2)	N(4)	2.052 (5)	C(27)	C(28)	1.39 (2)
		2.11 (1)			1.40 (2)
Mn(2)	N(5)	2.235 (6)	C(27)	C(32)	1.379 (9)
		2.23 (1)			1.41 (2)
Mn(2)	N(6)	2.073 (5)	C(28)	C(29)	1.37 (1)
		2.18 (1)			1.38 (2)
O(1)	C(35)	1.283 (7)	C(29)	C(30)	1.39 (2)
		1.31 (2)			1.40 (2)
O(2)	C(35)	1.219 (7)	C(29)	C(37)	1.57 (1)
		1.22 (2)			1.50 (2)
O(3)	C(33)	1.237 (8)	C(30)	C(31)	1.40 (2)
		1.21 (2)			1.38 (2)
O(4)	C(33)	1.280 (8)	C(31)	C(32)	1.397 (9)
		1.25 (2)			1.38 (2)
O(5)	C(32)	1.364 (7)	C(33)	C(34)	1.50 (2)
		1.36 (2)			1.54 (2)
N(1)	C(1)	1.355 (9)	C(35)	C(36)	1.53 (1)
		1.52 (2)			1.50 (2)
N(1)	C(5)	1.339 (8)	Cl(1)	O(6)	1.36 (2)
		1.53 (2)			1.40 (2)
N(2)	C(8)	1.343 (9)	Cl(1)	O(7)	1.35 (2)
		1.48 (2)			1.34 (1)
N(2)	C(12)	1.323 (9)	Cl(1)	O(8)	1.47 (2)
		1.52 (3)			1.41 (2)
N(3)	C(6)	1.455 (8)	Cl(1)	O(9)	1.36 (4)
		1.53 (2)			1.48 (2)
N(3)	C(7)	1.476 (9)	Cl(2)	Cl(10)	1.425 (2)
		1.52 (2)			1.46 (2)
N(3)	C(25)	1.502 (8)	Cl(2)	O(11)	1.421 (7)
		1.47 (2)			1.36 (2)
N(4)	C(20)	1.363 (9)	Cl(2)	O(12)	1.408 (7)
		1.48 (2)			1.39 (2)
N(4)	C(24)	1.327 (9)	Cl(2)	O(13)	1.412 (7)
		1.51 (2)			1.42 (1)
N(5)	C(13)	1.322 (8)			
		1.53 (2)			
		Additional Bond Distances for **1**			
C(1)	C(2)	1.37 (2)	C(13)	C(14)	1.40 (2)
C(2)	C(3)	1.39 (1)	C(14)	C(15)	1.35 (1)
C(3)	C(4)	1.37 (1)	C(15)	C(16)	1.39 (1)
C(4)	C(5)	1.377 (9)	C(16)	C(17)	1.38 (2)
C(8)	C(9)	1.393 (9)	C(20)	C(21)	1.37 (2)
C(9)	C(10)	1.37 (1)	C(21)	C(22)	1.36 (1)
C(10)	C(11)	1.35 (1)	C(22)	C(23)	1.37 (1)
C(11)	C(12)	1.40 (1)	C(23)	C(24)	1.37 (1)
		Additional Bond Distances for **2**			
C(1)	C(12)	1.47 (2)	C(13)	C(24)	1.52 (2)

[a] Numbers in parentheses are estimated standard deviations in the least significant digits.

from spin-forbidden absorptions whose allowedness has been increased because the total spin may be conserved for transitions

(24) König, E.; Kremer, S. *Ligand Field Energy Diagrams*; Plenum Press: New York, 1977; pp 175–200.

Table III. Selected Bond Angles (Degrees) for **1** and **2** (Values for **2** Are Listed below Those for **1**[a]

atom 1	atom 2	atom 3	angle	atom 1	atom 2	atom 3	angle
O(2)	Mn(1)	O(4)	93.7 (2)	Mn(1)	O(2)	C(35)	135.1 (5)
			100.2 (4)				131 (1)
O(2)	Mn(1)	O(5)	85.9 (2)	Mn(2)	O(3)	C(33)	140.3 (5)
			86.8 (4)				130.2 (9)
O(2)	Mn(1)	N(1)	169.7 (2)	Mn(1)	O(4)	C(33)	127.4 (4)
			162.7 (4)				130 (1)
O(2)	Mn(1)	N(2)	88.1 (2)	Mn(1)	O(5)	Mn(2)	114.4 (2)
			84.9 (4)				112.1 (4)
O(2)	Mn(1)	N(3)	99.6 (2)	Mn(1)	O(5)	C(32)	121.0 (3)
			93.7 (4)				120.8 (8)
O(4)	Mn(1)	O(5)	100.4 (2)	Mn(2)	O(5)	C(32)	123.7 (3)
			93.5 (4)				126.7 (9)
O(4)	Mn(1)	N(1)	92.1 (2)	Mn(1)	N(1)	C(1)	122.5 (4)
			88.0 (4)				110.2 (9)
O(4)	Mn(1)	N(2)	102.8 (2)	Mn(1)	N(1)	C(5)	115.6 (5)
			101.5 (5)				107.3 (8)
O(4)	Mn(1)	N(3)	166.2 (2)	C(1)	N(1)	C(5)	119.1 (6)
			166.1 (4)				112 (1)
O(5)	Mn(1)	N(1)	84.7 (2)	Mn(1)	N(2)	C(8)	116.2 (5)
			108.0 (4)				109.5 (9)
O(5)	Mn(1)	N(2)	156.4 (2)	Mn(1)	N(2)	C(12)	124.7 (5)
			163.9 (4)				103.0 (9)
O(5)	Mn(1)	N(3)	84.2 (2)	C(8)	N(2)	C(12)	119.1 (5)
			87.1 (4)				117 (1)
N(1)	Mn(1)	N(2)	99.0 (2)	Mn(1)	N(3)	C(6)	108.7 (4)
			78.6 (4)				113.1 (7)
N(1)	Mn(1)	N(3)	75.3 (2)	Mn(1)	N(3)	C(7)	105.1 (4)
			78.6 (4)				100.9 (7)
N(2)	Mn(1)	N(3)	74.3 (2)	Mn(1)	N(3)	C(25)	111.3 (3)
			79.7 (4)				111.1 (8)
O(1)	Mn(2)	O(3)	93.6 (2)	C(6)	N(3)	C(7)	109.4 (5)
			99.1 (4)				112 (2)
O(1)	Mn(2)	O(5)	99.1 (2)	C(6)	N(3)	C(25)	111.7 (5)
			98.1 (4)				110 (1)
O(1)	Mn(2)	N(4)	90.7 (2)	C(7)	N(3)	C(25)	110.5 (5)
			90.5 (4)				110 (1)
O(1)	Mn(2)	N(5)	91.0 (2)	Mn(2)	N(4)	C(20)	113.9 (4)
			87.2 (4)				110.4 (8)
O(1)	Mn(2)	N(6)	165.3 (2)	Mn(2)	N(4)	C(24)	126.7 (5)
			166.0 (4)				107.2 (8)
O(3)	Mn(2)	O(5)	93.4 (2)	C(20)	N(4)	C(24)	119.4 (6)
			91.5 (4)				113 (1)
O(3)	Mn(2)	N(4)	84.9 (2)	Mn(2)	N(5)	C(13)	124.8 (5)
			86.9 (4)				108.3 (8)
O(3)	Mn(2)	N(5)	175.4 (2)	Mn(2)	N(5)	C(17)	110.6 (4)
			166.2 (4)				105.2 (8)
O(3)	Mn(2)	N(6)	95.2 (3)	C(13)	N(5)	C(17)	119.1 (6)
			92.1 (4)				115 (1)
O(5)	Mn(2)	N(4)	170.2 (2)	Mn(2)	N(6)	C(18)	110.3 (4)
			171.5 (4)				110.1 (8)
O(5)	Mn(2)	N(5)	86.2 (2)	Mn(2)	N(6)	C(19)	105.4 (4)
			99.8 (4)				102.9 (8)
O(5)	Mn(2)	N(6)	92.1 (2)	Mn(2)	N(6)	C(26)	110.7 (4)
			90.0 (4)				109.7 (9)
N(4)	Mn(2)	N(5)	94.7 (2)	C(18)	N(6)	C(19)	109.6 (5)
			80.8 (4)				113 (1)
N(4)	Mn(2)	N(6)	78.4 (2)	C(18)	N(6)	C(26)	110.1 (5)
			81.7 (4)				111 (1)
N(5)	Mn(2)	N(6)	80.2 (2)	C(19)	N(6)	C(26)	110.7 (6)
			80.1 (4)				111 (1)
Mn(2)	O(1)	C(35)	133.5 (4)				
			133.5 (8)				

[a] Numbers in parentheses are estimated standard deviations in the least significant digits.

of a binuclear $Mn^{II}Mn^{III}$ complex.[25,26]

Description of the X-ray Structures. The structures of **1** and **2** are similar. Each contains dipositive, binuclear cations separated by perchlorate anions. The structure of complex **2** has, in addition, one disordered methylene chloride, whereas there is one disordered H_2O molecule in **1**. In both the $[Mn_2(bpmp)(\mu\text{-}OAc)_2]^{2+}$ cation in **1** (Figure 2, top) and the $[Mn_2(bcmp)(\mu\text{-}OAc)_2]^{2+}$ cation in **2** (Figure 2, bottom), the manganese ions are bridged by two

(25) Marzzaco, C. J.; McClure, D. S. *Symp. Faraday Soc., No. 3*, **1969**, 106–118.

(26) Schugar, H. J.; Rossman, G. B. R.; Barraclough, C. G.; Gray, H. B. *J. Am. Chem. Soc.* **1972**, *94*, 2683–2690.

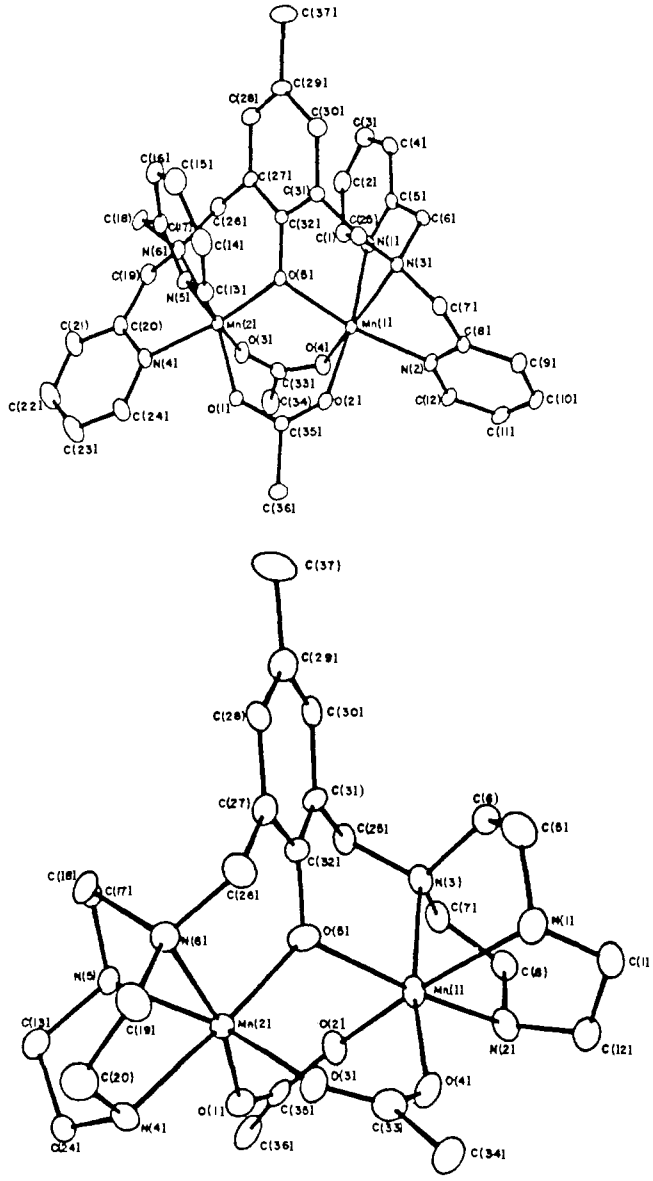

Figure 2. ORTEP plots of the (top) $[Mn_2(bpmp)(\mu\text{-}OAc)_2]^{2+}$ cation in complex **1** and (bottom) $[Mn_2(bcmp)(\mu\text{-}OAc)_2]^{2+}$ cation in complex **2**. Hydrogen atoms are not shown.

bidentate acetate groups and by the central phenoxy oxygen atom of the heptadentate bcmp$^-$ or bpmp$^-$ ligand. Three N-donor atoms from either arm of the heptadentate ligand coordinate facially and complete N_3O_3 coordination about each Mn atom. Bond lengths and angles for **1** and **2** are found in Table II and III, respectively.

In both structures, Mn(1) has a distorted octahedral coordination geometry with structural parameters typical of Mn^{II}. *cis*- and *trans*-L-Mn(1)-L′ angles span the ranges 74.3 (2)-108.0 (4)° and 156.4 (2)-169.7 (2)°, respectively; the *cis*-N-Mn(1)-N angles are typically the smallest, presumably because of constraints imposed by the polydentate ligands. The Mn(1)-O distances range from 2.066 (5) to 2.193 (4) Å. They fall within the range reported previously for several Mn^{II} complexes[27] and compare favorably with those observed for other binuclear manganese complexes containing octahedrally coordinated Mn^{II} (Table IV). Interestingly, in both of the present structures, as well as in the benzoate[9] and imidazole[10] analogues of **1** (Table IV), the Mn(1)-O(phenoxy) length is longer than either Mn(1)-O(carboxylate) length, although the opposite might have been expected from static

Table IV. Structural Comparisons[a] for $Mn^{II}Mn^{III}$ Complexes Containing Heptadentate N_6O Ligands

	1[b]	**2**[c]	**3**[d]	**4**[e]
$Mn^{II}\cdots Mn^{III}$	3.447 (1)	3.422 (3)	3.483 (3)	3.54 (1)
Mn^{II}-O(phenoxy)-Mn^{III}	114.4 (2)	121.1 (4)	116.6 (5)	116.8 (3)
		Mn^{II}		
Mn^{II}-O(phenoxy)	2.193 (4)	2.17 (1)	2.184 (9)	2.258 (6)
Mn^{II}-N(imine)[f]	2.271 (6)	2.26 (1)	2.273 (12)	2.186 (7)
Mn^{II}-N(imine)	2.210 (6)	2.22 (1)	2.224 (12)	2.229 (7)
Mn^{II}-N(amine)[g]	2.324 (5)	2.23 (1)	2.304 (13)	2.364 (6)
Mn^{II}-O(carboxylate)	2.166 (4)	2.135 (9)	2.162 (11)	2.107 (6)
Mn^{II}-O(carboxylate)	2.066 (5)	2.09 (1)	2.123 (11)	2.091 (6)
		Mn^{III}		
Mn^{III}-O(phenoxy)	1.903 (4)	1.957 (9)	1.905 (10)	1.887 (5)
Mn^{III}-N(imine)[f]	2.052 (5)	2.11 (1)	2.022 (14)	1.998 (7)
Mn^{III}-N(imine)[h]	2.235 (6)	2.23 (1)	2.217 (12)	2.100 (7)
Mn^{III}-N(amine)[g]	2.073 (5)	2.18 (1)	2.110 (12)	2.270 (8)
Mn^{III}-O(carboxylate)	1.927 (5)	2.01 (1)	1.947 (10)	1.995 (6)
Mn^{III}-O(carboxylate)[h]	2.090 (4)	2.056 (9)	2.147 (11)	2.036 (8)

[a] Bond distances are in angstroms, bond angles in degrees. [b] **1** = $[Mn_2(bpmp)(\mu\text{-}OAc)_2]\cdot(ClO_4)_2\cdot H_2O$; this work. [c] **2** = $[Mn_2(bcmp)(\mu\text{-}OAc)_2]\cdot(ClO_4)_2\cdot CH_2Cl_2$; this work. [d] **3** = $[Mn_2(bpmp)(\mu\text{-}OBz)_2]\cdot(ClO_4)_2\cdot H_2O$; ref 9. [e] **4** = $[Mn_2(L\text{-}im)(\mu\text{-}OAc)_2\cdot(ClO_4)_2$; ref 10a:

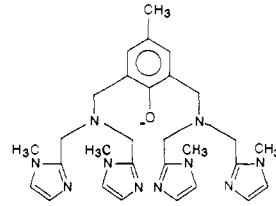

[f] Nitrogen atom trans to $Mn^{II}\cdots O$(phenoxy). [g] N(amine) refers to the tertiary amine N atoms in bpmp, bcmp, and L-im. N(imine) refers to the remaining N atoms of the heptadentate ligands. [h] Lengthened by Jahn-Teller effect.

charge considerations alone. The Mn(1)-N distances [2.210 (6)-2.324 (5) Å] lie within the range reported[27] for Mn^{II}-N lengths. In the bcmp derivative **2**, which contains macrocyclic triazacyclononane groups, the Mn^{II}-N distances vary only slightly [2.23 (1)-2.26 (1) Å]. In contrast, complex **1** and the benzoate and imidazole analogues of **1**, which have pendant N(imine) and N(amine) ligating atoms, all exhibit Mn(1)-N(amine) distances that are significantly longer than the corresponding Mn(1)-N(imine) distances. On the basis of the available structural data, it is not clear whether these differences arise from differences in basicities of the various nitrogen-donor ligands or from steric constraints imposed by the heptadentate ligands.

In structures **1** and **2**, the second manganese ion, Mn(2), shows structural parameters consistent with its assignment as Mn^{III} with a distorted octahedral coordination geometry. Here, in contrast to Mn(1), the Mn(2)-O(phenoxy) distance [Mn(2)-O(5)] is shorter than either Mn(2)-O(carboxylate) distance, while the Mn(2)-N(imine) distance trans to Mn(2)-O(5) is shorter than the other two Mn-N distances. This pattern is also present in the benzoate[9] and imidazole[10] analogues of **1** as well as in the binuclear oxo-bridged manganese(III) complex $[Mn_2O(\mu\text{-}OAc)_2(HB(pz)_3)_2]$[6n], where $HB(pz)_3$ is the tridentate N_3 ligand hydrotris(1-pyrazolyl) borate. In this latter structure, shortening of the *trans*-Mn^{III}-N distance was rationalized by assuming that the short Mn^{III}-O(oxo) distance raises the energy of the d_{z^2} orbital (where z is the direction of the Mn^{III}-O(oxo) bond) to such an extent that it is empty for the high-spin d^4 Mn^{III} ion, permitting the close approach of a trans ligand. This interpretation is consistent with the very weak antiferromagnetic coupling (J = -0.5 cm^{-1}) observed in the $Mn_2^{III}O$ complex. A related binuclear oxo-bridged manganese complex,[6d] $[Mn_2^{III}O(\mu\text{-}OAc)_2L_2]^{2+}$, where L = 1,4,7-triazacyclononane, shows a similar trans shortening. However, the structure of $[Mn_2^{III}O(\mu\text{-}OAc)_2(H_2O)_2(bipy)_2]^{2+}$, where bipy = 2,2′-bipyridine,[28] shows no shortening of the Mn^{III}-N

(27) Mabad, B.; Cassoux, P.; Tuchagues, J.-P.; Hendrickson, D. N. *Inorg. Chem.* **1986**, *25*, 1420-1431.

(28) Menage, S.; Girerd, J.-J.; Gleizes, A. *J. Chem. Soc., Chem. Commun.* **1988**, 431-432.

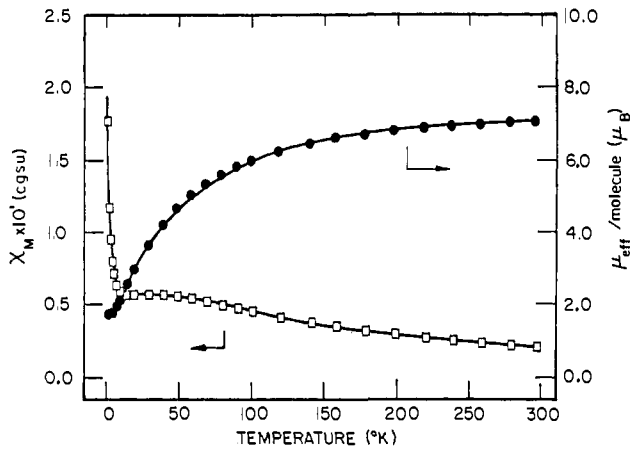

Figure 3. Molar paramagnetic susceptibility per complex, χ_M, and effective magnetic moment per molecule, μ_{eff}/molecule, versus temperature for $[Mn_2(bpmp)(\mu\text{-}OAc)_2](ClO_4)_2 \cdot H_2O$ (**1**). The solid lines represent the least-squares fit of the data to eq 1. See text for parameters.

bond trans to the Mn–O(oxo) bond. The bipy complex exhibits a weak antiferromagnetic coupling (J = −6.8 cm^{-1}) that is somewhat stronger than that in the $HB(pz)_3$ complex. The coordination geometry of Mn(2) is further distorted by the inequivalence of the Mn(2)O(carboxylate) distances and the Mn(2)–N distances trans to them. The Mn(2)–O(3) and Mn(2)–N(5) distances are relatively long, consistent with the Jahn–Teller distortion expected for high-spin d^4 Mn^{III} complexes.

On the basis of the structural data, the cations in **1** and **2** are clearly valence-trapped $Mn^{II}Mn^{III}$ species. They are further characterized by the Mn···Mn distances and Mn^{II}–O(phenoxy)–Mn^{III} angles (Table IV) which are quite similar for **1** [3.447 (1) Å, 114.4 (2)°], **2** [3.422 (3) Å, 121.1 (4)°], the benzoate derivative of **1** [3.483 (3) Å, 116.6 (5)°], and the imidazole derivative of **1** [3.54 (1) Å, 116.8 (3)°].

NMR Spectra of the Complexes. The 400-MHz ^1H NMR spectra of binuclear complexes **1** in CH_2Cl_2-d_2 and **2** in CH_3CN-d_3 were determined (spectra are given in the supplementary material (see paragraph at the end of the paper)). The NMR spectrum of **1** consists of several broad and sharp signals between −30 to +60 ppm. No reliable integration of the signals could be obtained because of the broadness of the peaks. Deuteration of the acetate bridges in **1** resulted in partial reduction in the peak heights for the two signals at 2 and 58 ppm. It is not clear if the signal at 2 ppm results from decomposition during the NMR measurements or from the bridged acetate group in the complex.

The NMR spectrum of complex **2** measured from 60 to −30 ppm shows signals only between +58 and 0 ppm. The NMR signals were observed in the upfield region. Deuteration of the acetate bridges in **2** caused partial reduction in the peak heights at 2 and 58 ppm. The absence of signals in the upfield region for **2** makes it possible to assign the pyridine protons of **1** to the peaks at −8.0, −12, and −22 ppm (vs TMS), since the main structural difference between **1** and **2** is the substitution of pyridine for the saturated amine in triazacyclononane.

Magnetic Susceptibility Data. Solid-state magnetic susceptibility data for complex **1** were collected from 298 to 2.2 K. As can be seen in Figure 3, the value of μ_{eff}/molecule varies from 7.13μ_B at 298 K to 1.76μ_B below 4.08 K. The effective magnetic moment per complex at 298 K is somewhat less than 7.68μ_B, which is the effective magnetic moment expected for a binuclear $Mn^{II}Mn^{III}$ complex with no magnetic exchange interaction between two spin-only centers ($S_1 = {}^5/_2$ and $S_2 = 2$). These results indicate that complex **1** has a doublet ground state ($S_T = {}^1/_2$) and that the two manganese centers (Mn^{II} and Mn^{III}) are high spin and have an antiferromagnetic exchange interaction between them. The spin Hamiltonian that describes the isotropic magnetic exchange interaction in such a binuclear complex is $H = -2JS_1 \cdot S_2$ and gives for the molar paramagnetic susceptibility

$$\chi_M = (Ng^2\beta^2)(1 + 10e^{3x} + 35e^{8x} + 84e^{15x} + 165e^{24x})/[(4kT)(1 + 2e^{3x} + 3e^{8x} + 4e^{15x} + 5e^{24x})] + \text{TIP} \quad (1)$$

In eq 1, $x = J/kT$, g is the average g value, TIP is the temperature independent paramagnetism, and the other symbols have their usual meanings. The paramagnetic susceptibility data for **1** were least-squares fit to eq 1 to give the fitting parameters J = −6.0 cm^{-1} and g = 1.98 with TIP held constant at 400 × 10^{-6} cgsu. The solid lines in Figure 3 represent this fit. Experimental and calculated susceptibility data are available in the supplementary material.

There are five states for a binuclear complex with $S_1 = {}^5/_2$ and $S_2 = 2$. These five states have total spin values of $S_T = {}^1/_2$, ${}^3/_2$, ${}^5/_2$, ${}^7/_2$, and ${}^9/_2$. If a Boltzmann distribution is assumed for complex **1** with J = −6.0 cm^{-1}, the occupancy of each of the five energy states at different temperatures can be calculated. At 7.5 K, the ground doublet state ($S_T = {}^1/_2$) has a ~94% occupancy and the first excited quartet state ($S_T = {}^3/_2$) has only a ~6% occupancy. When the temperature is increased to 15 K, the occupancy of the quartet state increases from ~6% to ~26%, and the population of the second excited state ($S_T = {}^5/_2$) increases from zero to ~2% occupancy, whereas the occupancy of the ground state decreases to ~72%. When the temperature is further increased, the thermal population of even higher energy excited states begin to increase. The occupancy for each energy state at a variety of temperatures will be used to discuss the temperature-dependent EPR spectra in the following EPR section.

Solid-state magnetic susceptibility data were measured for complex **2** from 301.16 to 5 K (figure in supplementary material). The value of μ_{eff}/molecule varies from 7.15μ_B at 301.16 K to 1.81μ_B at 5 K. The paramagnetic susceptibility data for **2** were least-squares fit to eq 1 to give the fitting parameters J = −7.7 cm^{-1} and g = 2.02 with TIP held constant at 400 × 10^{-6} cgsu. Experimental and calculated data are available in the supplementary material. Boltzmann distributions were also calculated for complex **2**. At 7.4 K, the ground state ($S_T = {}^1/_2$) of complex **2** has a ~98% occupancy, which is more than that in complex **1** (~94%), as is expected for a complex with a larger antiferromagnetic interaction. The first excited state ($S = {}^3/_2$) of **2** has only a 2.3% occupancy at 7.5 K, while when the temperature is increased to 30 K, the occupancies (state S_T) are 0.8% (${}^7/_2$), 8.4% (${}^5/_2$), 36.0% (${}^3/_2$), and 54.8% (${}^1/_2$).

In addition to the two complexes reported in this work, four other structurally characterized $Mn^{II}Mn^{III}$ complexes are known.[9,10,30,31] Magnetic exchange parameters in the range of +0.89 to −6.3 cm^{-1} have been found for these complexes.

There are also seven structurally characterized binuclear $Mn^{III}Mn^{IV}$ complexes known.[29,32-36] The antiferromagnetic exchange interactions for the $Mn^{II}Mn^{III}$ complexes are quite weak relative to those for the $Mn^{III}Mn^{IV}$ complexes. In the former case J ranges from −7.7 to +0.89 cm^{-1}. In the latter case J ranges from −40 to −220 cm^{-1}. There are perhaps two possible explanations for why the antiferromagnetic interactions observed for the $Mn^{III}Mn^{IV}$ complexes are greater than those observed for the

(29) Li, Q.; Oberhausen, K. J.; Richardson, J. F.; Buchanan, R. M.; Hendrickson, D. N., manuscript in preparation.

(30) Baskin, J. S.; Schake, A. R.; Vincent, J. B.; Huffman, J. C.; Christou, G.; Chang, H.-R.; Li, Q.; Hendrickson, D. N. *J. Chem. Soc., Chem. Commun.* **1988**, 700–702.

(31) Chang, H.-R.; Larsen, S.; Pierpont, C. G.; Boyd, P. D. W.; Hendrickson, D. N. *J. Am. Chem. Soc.* **1988**, *110*, 4565–4576.

(32) (a) Wieghardt, K.; Bossek, U.; Bonvoisin, J.; Beauvillain, P.; Girerd, J.-J.; Nuber, B.; Weiss, J.; Heinze, J. *Angew. Chem., Int. Ed. Engl.* **1986**, *25*, 1030–1031. (b) Weighardt, K.; Bossek, U.; Zsolnai, L.; Huttner, G.; Blondin, G.; Girerd, J.-J.; Babonneau, F. *J. Chem. Soc., Chem. Commun.* **1987**, 651–653.

(33) Siebler, M.; Ludi, A.; Bürgi, H.-B. *Inorg. Chem.* **1986**, *25*, 4743–4750.

(34) Collins, M. A.; Hodgson, D. J.; Michelsen, K.; Towle, D. K. *J. Chem. Soc., Chem. Commun.* **1987**, 1659–1661.

(35) (a) Plaskin, P. M.; Stoufer, R. C.; Mathew, M.; Palenik, G. J. *J. Am. Chem. Soc.*, **1972**, *94*, 2121. (b) Cooper, S. R.; Dismukes, G. C.; Klein, M. P.; Calvin, M. *J. Am. Chem. Soc.* **1978**, *100*, 7248.

(36) Hagen, K. S.; Armstrong, W. H.; Hope, H. *Inorg. Chem.* **1988**, *27*, 969–971.

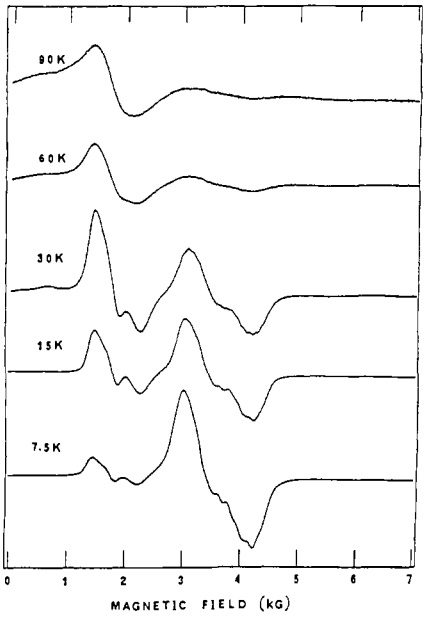

Figure 4. Variable-temperature X-band EPR spectra for a polycrystalline sample of $[Mn_2(bpmp)(\mu\text{-}OAc)_2](ClO_4)_2\cdot H_2O$ (**1**).

$Mn^{II}Mn^{III}$ complexes. First, in converting a $Mn^{III}Mn^{IV}$ complex to a $Mn^{II}Mn^{III}$ complex two e_g*-type d electrons are added to one metal center, and if everything else remained the same, the presence of these two additional d electrons would likely increase the number of ferromagnetic exchange pathways relative to the number of antiferromagnetic exchange pathways.[37] Thus, the interactions between the e_g*-type magnetic orbitals on the Mn^{II} ion and the t_{2g}-type magnetic orbitals on the Mn^{III} ion, as propagated by $2p_x$, $2p_y$, and $2p_z$ oxygen orbitals, will largely be orthogonal and, consequently, ferromagnetic in origin. Second, for those $Mn^{III}Mn^{IV}$ complexes that are *not* disordered in the solid state the Mn^{III}–O (bridge) bond lengths are only 0.04–0.07 Å longer than the Mn^{IV}–O bond lengths.[33] In contrast, the Mn^{II}–O (bridge) bond lengths in the structurally characterized $Mn^{II}Mn^{III}$ complexes are appreciably larger than the Mn^{III}–O (bridge) bond lengths. The Mn^{II}–O bond lengths fall in the range 2.17–2.39 Å, whereas the Mn^{III}–O bond lengths are in the range 1.83–1.85 Å. It is likely that this appreciable difference in Mn^{II}–O and Mn^{III}–O bond lengths would lead to weak antiferromagnetic interactions for the $Mn^{II}Mn^{III}$ complexes.

Experimental and Simulated X- and Q-band EPR Spectra of Complexes 1 and 2. Variable-temperature first-derivative X-band EPR spectra for a microcrystalline sample of **1** are shown in Figure 4. The relative intensity of the signal at $g \simeq 2$ decreases, but that at half-field ($g \simeq 4$) increases when the sample temperature is increased. It is likely that the signal at $g \simeq 2$ is largely due to complexes in the $S_T = {}^1/_2$ ground state, and the signal at $g \simeq 4$ is due to complexes in the $S_T = {}^3/_2$ quartet excited state. (A figure showing similar EPR data for **2** is given in the supplementary material).

The spin Hamiltonian[38] for a complex in the $S_T = {}^3/_2$ excited state is given in eq 2, where the complex is assumed to have axial

$$\hat{H} = \beta g_\parallel \hat{H}_z \hat{S}_z + \beta g_\perp (\hat{H}_x \hat{S}_x + \hat{H}_y \hat{S}_y) + A_\parallel \hat{I}_z \hat{S}_z + A_\perp (\hat{I}_x \hat{S}_x + \hat{I}_y \hat{S}_y) + D[\hat{S}_z^2 - {}^1/_3 S(S+1)] \quad (2)$$

symmetry. If we neglect the hyperfine interaction term and apply the condition $D \gg g\beta H$, then the energies of the two Kramers doublets of a $S_T = {}^3/_2$ state are given as

$$E_{\pm 3/2} = D \pm {}^3/_2 g_\parallel \beta H \cos\theta$$

$$E_{\pm 1/2} = -D \pm (\beta H/2)(g_\parallel^2 \cos^2\theta + 4g_\perp^2 \sin^2\theta)^{1/2} \quad (3)$$

where θ is the angle between the principal magnetic axis and the externally applied magnetic field. Thus, the **g** tensors for the transitions $E_{+3/2} \leftrightarrow E_{-3/2}$ and $E_{+1/2} \leftrightarrow E_{-1/2}$ are

$$E_{+3/2} \leftrightarrow E_{-3/2}: \quad g'_\parallel = 3g_\parallel \cong 6.0; \quad g'_\perp \cong 0$$

$$E_{+1/2} \leftrightarrow E_{-1/2}: \quad g'_\parallel = g_\parallel \cong 2.0; \quad g'_\perp = 2g_\perp \cong 4.0 \quad (4)$$

where the primes indicate the effective g values. If D is positive and larger than the applied microwave energy ($D \gg h\nu$), the $M_S = \pm{}^1/_2$ Kramers doublet is the lower energy level of the two doublets. Thus, at low temperatures only the transition between the $M_S = \pm{}^1/_2$ levels is observable.

In these binuclear complexes, the D value for the $S_T = {}^3/_2$ quartet state reflects the single-ion zero-field splittings of the Mn^{II} and Mn^{III} ions, D_1 and D_2, respectively. Octahedral Mn^{II} complexes generally have D values less than $\sim+0.1$ cm^{-1}, whereas if the octahedral coordination geometry becomes tetragonally elongated, D will become as large as $\sim+1$ cm^{-1}, because the energy difference between the $^6A_1$ and $^4T_1$ states is reduced relative to the octahedral Mn^{II} case.[39] D values for Schiff-base and porphyrin complexes of Mn^{III} have been found[40] to fall in the range of -1.0 to -3.0 cm^{-1}. The ground state for a C_{4v} symmetry Mn^{III} complex is $^5B_1$, and if $D < 0$ this means the $M_S = \pm 2$ level is at the lowest energy.

Since the binuclear complexes **1** and **2** have small negative J values, the g values for the three Kramers doublets from the $S_T = {}^1/_2$ and ${}^3/_2$ states are sensitive to the values of D_1 and D_2. In a previous paper[31] we derived the 30 × 30 Hamiltonian energy matrix for a d^4–d^5 system including the effects of an isotropic magnetic exchange interaction, single-ion zero-field interactions, and an axially symmetric Zeeman interaction. For complexes **1** and **2**, since the energy separations (>18 cm^{-1} between each pair) between the five energy states are reasonably larger than the D values in each for the excited states, the five spin states do not have too much interaction between each other to complicate a EPR spectrum. However, even small values of the single-ion zero-field splitting parameters of D_1 and D_2 will affect $g_\perp$ for the $S = {}^1/_2$ ground state. The full 30 × 30 Hamiltonian matrix was diagonalized with $J = -6.0$ cm^{-1} held constant while D_1 and D_2 were varied. Table V lists the values of $g_\parallel$ and $g_\perp$ for the transition in the doublet ground state as $g_\parallel{}^1$, $g_\perp{}^1$, and the possible transitions in the quartet excited state ($|{}^3/_2,{}^1/_2\rangle \leftrightarrow |{}^3/_2,{}^{-1}/_2\rangle$ and $|{}^3/_2,{}^3/_2\rangle \leftrightarrow |{}^3/_2,{}^{-3}/_2\rangle$). The g values for the Kramers doublet of the $S = {}^3/_2$ state that is closer in energy to the $S_T = {}^1/_2$ ground state are given as $g_\parallel{}^2$, $g_\perp{}^2$ and the g values for the other one as $g_\parallel{}^3$, $g_\perp{}^3$.

From Table V it can be seen that the $g_\parallel$ values of all three low-lying Kramers doublets are not affected by the values of D_1 and D_2. The $g_\parallel$ values stay as 2.0 for the $|{}^1/_2,{}^1/_2\rangle \leftrightarrow |{}^1/_2,{}^{-1}/_2\rangle$ and $|{}^3/_2,{}^1/_2\rangle \leftrightarrow |{}^3/_2,{}^{-1}/_2\rangle$ transitions and as 6.0 for the $|{}^3/_2,{}^3/_2\rangle \leftrightarrow |{}^3/_2,{}^{-3}/_2\rangle$ transition (this last one is usually a forbidden transition). On the other hand, the values of $g_\perp$ for the three doublets vary as a result of changes in the magnitudes of D_1 and D_2. If the sign of the zero-field splitting (D) in the quartet state is positive, then the $|{}^3/_2,{}^1/_2\rangle$ and $|{}^3/_2,{}^{-1}/_2\rangle$ states are close to the $S = {}^1/_2$ ground state. The $|{}^3/_2,{}^3/_2\rangle$ and $|{}^3/_2,{}^{-3}/_2\rangle$ states will be at lower energy than the $|{}^3/_2,\pm{}^1/_2\rangle$ Kramers doublet states when $|D_2| < 0.5$ cm^{-1} and $|D_1| > 0.0$ cm^{-1}. From Figure 4 it is not possible to tell whether the D value for the quartet state is positive or negative, since the $|{}^3/_2,{}^3/_2\rangle \leftrightarrow |{}^3/_2,{}^{-3}/_2\rangle$ transition is forbidden and the energy gap between the doublet ground state and the excited quartet state is much larger than the zero-field splitting in the quartet state.

With reference to the EPR spectra in Figure 4 there are several features that must be mentioned and discussed: (i) the bump at

(37) Ginsberg, A. P. *Inorg. Chim. Acta* **1971**, *5*, 45–68.
(38) Abragam, A.; Bleaney, B. *Electron Paramagnetic Resonance of Transition Ions*; Oxford Press: Oxford, 1970.

(39) (a) Yonetani, T., et al., *J. Biol. Chem.* **1970**, *245*, 2998. (b) Dowsing, R. D.; Gibson, J. F.; Goodgame, M.; Hayward, P. J. *J. Chem. Soc. A* **1970**, 1133–1138. (c) Birdy, R. B.; Goodgame, M. G. *J. Chem. Soc., Dalton Trans.* **1983**, 1469–1471.
(40) (a) Dugad, L. B.; Behere, D. V.; Marathe, V. R.; Mitra, S. *Chem. Phys. Lett.* **1984**, *104*, 353–356. (b) Kennedy, B. J.; Murray, K. S. *Inorg. Chem.* **1985**, *24*, 1552–1557, 1557–1560. (c) Mathe, J.; Schinkel, C. J.; VanAnsted, W. A. *Chem. Phys. Lett.* **1975**, *33*, 528–531. (d) Behere, D. V.; Marathe, V. R.; Mitra, S. *Chem. Phys. Lett.* **1981**, *81*, 57–61, and references therein.

Table V. Expected Values of $g_\parallel$ and $g_\perp$ Calculated for a Binuclear $Mn^{II}Mn^{III}$ Complex with $J = -6$ cm^{-1} and Various Values of D_1 (cm^{-1}) and D_2 (cm^{-1})[a]

		D_2					
D_1		0.00	−0.5	−1.0	−2.0	−3.0	−4.0
0.0	$g_\parallel^1$	2.00	2.00	2.00	2.00	2.00	2.00
	$g_\perp^1$	2.00	2.00	1.99	1.97	1.92	1.85
	$g_\parallel^2$	2.00	2.00	2.00	2.00	2.00	2.00
	$g_\perp^2$	2.00	3.78	3.99	3.95	3.88	3.78
	$g_\parallel^3$	2.00	6.00	6.00	6.00	6.00	6.00
	$g_\perp^3$	2.00	0.22	0.00	0.00	0.00	0.00
0.2	$g_\parallel^1$	2.00	2.00	2.00	2.00	2.00	2.00
	$g_\perp^1$	2.00	2.00	2.00	1.99	1.95	1.90
	$g_\parallel^2$	6.00	2.00	2.00	2.00	2.00	2.00
	$g_\perp^2$	0.02	3.73	4.00	3.97	3.91	3.82
	$g_\parallel^3$	2.00	6.00	6.00	6.00	6.00	6.00
	$g_\perp^3$	3.98	0.27	0.00	0.00	0.00	0.00
0.4	$g_\parallel^1$	2.00	2.00	2.00	2.00	2.00	2.00
	$g_\perp^1$	1.99	2.00	2.00	2.00	1.98	1.94
	$g_\parallel^2$	6.00	2.00	2.00	2.00	2.00	2.00
	$g_\perp^2$	0.00	3.63	4.00	3.98	3.94	3.87
	$g_\parallel^3$	2.00	6.00	6.00	6.00	6.00	6.00
	$g_\perp^3$	3.98	0.36	0.00	0.00	0.00	0.00
0.6	$g_\parallel^1$	2.00	2.00	2.00	2.00	2.00	2.00
	$g_\perp^1$	1.98	1.99	2.00	2.01	2.00	1.97
	$g_\parallel^2$	6.00	2.00	2.00	2.00	2.00	2.00
	$g_\perp^2$	0.00	3.45	3.99	3.99	3.96	3.90
	$g_\parallel^3$	2.00	6.00	6.00	6.00	6.00	6.00
	$g_\perp^3$	3.97	0.53	0.00	0.00	0.00	0.00
0.8	$g_\parallel^1$	2.00	2.00	2.00	2.00	2.00	2.00
	$g_\perp^1$	1.96	1.97	1.99	2.01	2.01	2.00
	$g_\parallel^2$	6.00	2.00	2.00	2.00	2.00	2.00
	$g_\perp^2$	0.43	3.09	3.85	3.96	3.96	3.92
	$g_\parallel^3$	2.00	4.60	6.00	6.00	6.00	6.00
	$g_\perp^3$	3.52	0.87	0.12	0.02	0.01	0.01
1.0	$g_\parallel^1$	2.00	2.00	2.00	2.00	2.00	2.00
	$g_\perp^1$	1.94	1.95	1.97	2.00	2.02	2.02
	$g_\parallel^2$	6.00	0.99	2.00	2.00	2.00	2.00
	$g_\perp^2$	0.27	2.46	3.79	3.95	3.96	3.94
	$g_\parallel^3$	2.00	3.01	6.00	6.00	6.00	6.00
	$g_\perp^3$	3.66	1.48	0.17	0.03	0.01	0.01

[a] $g_\parallel^1$, $g_\perp^1$ are the g values of $|^1/_2, {}^1/_2\rangle \leftrightarrow |^1/_2, {}^{-1}/_2\rangle$ transition in doublet ground state. $g_\parallel^2$, $g_\perp^2$ are the g values of lower energy transition ($|^3/_2, {}^3/_2\rangle \leftrightarrow |^3/_2, {}^{-3}/_2\rangle$ or $|^3/_2, {}^1/_2\rangle \leftrightarrow |^3/_2, {}^{-1}/_2\rangle$) in quartet state. $g_\parallel^3$, $g_\perp^3$ are the g values of higher energy transition ($|^3/_2, {}^3/_2\rangle \leftrightarrow |^3/_2, {}^{-3}/_2\rangle$ or $|^3/_2, {}^1/_2\rangle \leftrightarrow |^3/_2, {}^{-1}/_2\rangle$) in quartet state.

$\sim$2000 G ($g \sim 3$) keeps a constant intensity relative to the signal at $\sim$1500 G ($g \sim 4$) as the temperature is increased from 7.5 to 30 K. The $g \sim 4$ signal is believed to belong to the transition between the $|^3/_2, {}^1/_2\rangle$ and $|^3/_2, {}^{-1}/_2\rangle$ components of the quartet state. The appearance of the two signals at $g \sim 3$ and $g \sim 4$ could be due to a rhombic distortion ($E \neq 0$) in the quartet state. The effects of rhombicity have been seen in a series of tetragonal Cr^{III} complexes studied by Pedersen and Toftlund.[41] A small amount of contribution from rhombic zero-field splitting results in splitting the $g_\perp$ signal into g_x and g_y signals. (ii) The complicated signal running from $\sim$2700 to $\sim$4600 G could result from the superposition of signals from the weak $g \sim 2$ signal of the $S = {}^3/_2$ state and the rhombic g_x, g_y, and g_z signals from the $S = {}^1/_2$ ground state. In Table VI it is shown that $g_\perp$ varies in response to a change in the single-ion D values. (iii) When the sample temperature is increased to $\sim$30 K, a new signal at $\sim$750 G ($g \sim 8$) appears. This signal is possibly due to the $|^5/_2, {}^1/_2\rangle \leftrightarrow |^5/_2, {}^{-1}/_2\rangle$ transition within the $S_T = {}^5/_2$ spin state. The Boltzmann population of the $S_T = {}^5/_2$ excited state is only $\sim$2% at 15 K and then increases to $\sim$13.8% at 30 K. Thus, only at 30 K will molecules in this state show an appreciable EPR signal.

The single-integration (absorption plot) and double-integration X-band EPR spectra for complex **1** are shown in Figure 5. At 7.5 K the relative intensities of the signals at $g = 2$ and $g = 4$ are 93% and $\sim$7%, respectively, which is in good agreement with the results of the magnetochemistry ($\sim$94% occupancy for the $S = {}^1/_2$ state and $\sim$6% occupancy for the $S = {}^3/_2$ state). At 15 K, the double-integrated spectrum for **1** shows $\sim$75% of the absorption signal at $g = 2$ and $\sim$25% at $g = 4$. These values are a little off from the magnetochemistry results ($\sim$72% for $S = {}^1/_2$, $\sim$26% for $S = {}^3/_2$ and $\sim$2% for $S = {}^5/_2$). This small difference is possibly attributable to the fact that the $S_T = {}^5/_2$ spin state could also give a signal in the $g = 2$ region. Furthermore, at even higher temperatures, the higher energy spin states are populated significantly (such as the $S = {}^5/_2$, ${}^7/_2$, and ${}^9/_2$ states), and those spin states could give EPR signals across the magnetic field range studied.

(41) Pedersen, E.; Toftlund, H. *Inorg. Chem.* **1974**, *13*, 1603.

Table VI. Hyperfine Coupling Constants Observed for Mn^{II}, Mn^{III}, and Mn^{IV} Ions in Six-Coordinate O_6 Host Sites

host	ox state	A_0	$A_\perp$	$A_\parallel$	ref
TiO_2	Mn^{IV}	71.6	72.6	70.3	43
	Mn^{III}	72.3	82.0	52.8	42
	Mn^{II}	−77	−77	−77	42
Al_2O_3	Mn^{IV}	−70.2	−70.6	−69.6	45
	Mn^{II}	−79.1	−78.8	−79.6	44
MgO	Mn^{IV}	−70.8	−70.6	−71.1	46
	Mn^{II}	−81.5	−81.5	−81.5	47

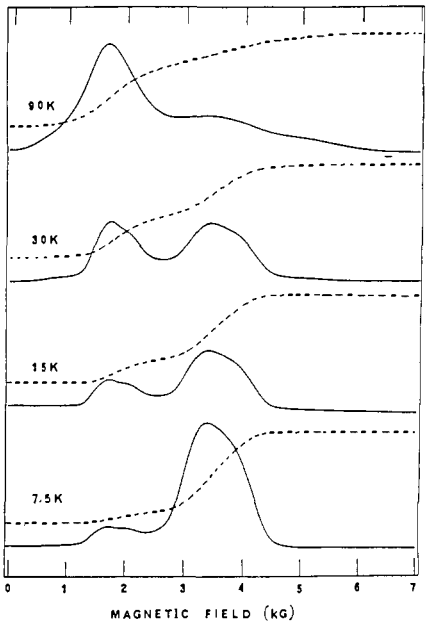

Figure 5. Variable-temperature single-integration (absorption plots as solid lines) and double-integration (dashed lines) X-band EPR spectra for $[Mn_2(bpmp)(\mu\text{-}OAc)_2](ClO_4)_2{\cdot}H_2O$ (**1**). The first-derivative EPR spectra shown in Figure 8 were integrated to obtain these plots.

The temperature dependence of the first-derivative X-band EPR spectra for a polycrystalline sample of complex **2** is similar to that for complex **1**; however, complex **2** shows less bumps in the $g \cong 2$ region than does complex **1**. It has been noted above that a rhombic **g** tensor for the $S_T = {}^1/_2$ ground state may be the origin of these bumps in the $g \cong 2$ region. Fewer bumps in the spectrum of complex **2** indicates that the **g** tensor of complex **2** may be more isotropic than in **1**. Support for this comes from the results of the X-ray structures, where it is seen that the Mn^{III} site has less Jahn–Teller distortion in **2** than in **1**.

Figure 6 shows the variable-temperature X-band EPR spectra for a frozen glass (2:1:2 acetone/toluene/ethanol) sample of complex **1**. A figure showing similar spectra for complex **2** is available in the supplementary material. The overall spectra are similar to those for the solid samples (Figure 4), except that in the glass spectra there are 29 well-resolved manganese hyperfine features associated with the $g \cong 2$ signal. Obviously, the 29-line manganese hyperfine pattern results from molecules in the $S = {}^1/_2$ ground state. For a binuclear complex with two equivalent ^{55}Mn nuclei (valence-detrapped or electronically delocalized) and an isotropic **g** tensor for the $S = {}^1/_2$ ground state, a maximum of 11 manganese hyperfine lines will be seen. If the $S_T = {}^1/_2$

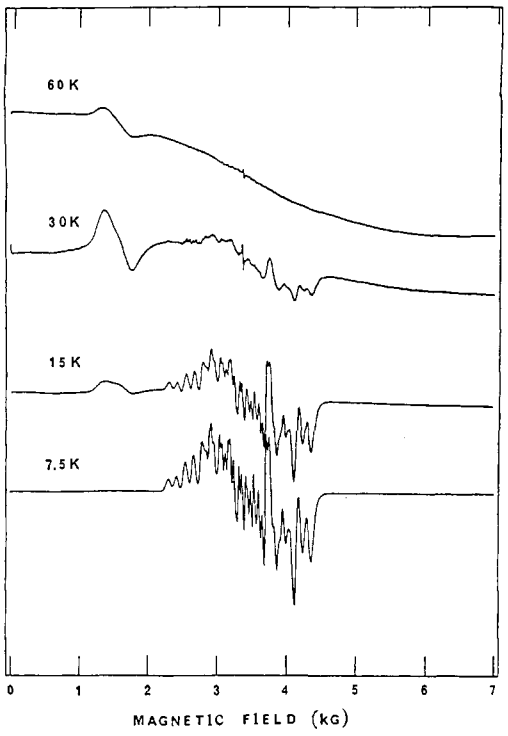

Figure 6. Variable-temperature X-band EPR spectra for an acetone/toluene/ethanol (2:1:2) frozen glass of $[Mn_2(bpmp)(\mu\text{-}OAc)_2](ClO_4)_2 \cdot H_2O$ (**1**).

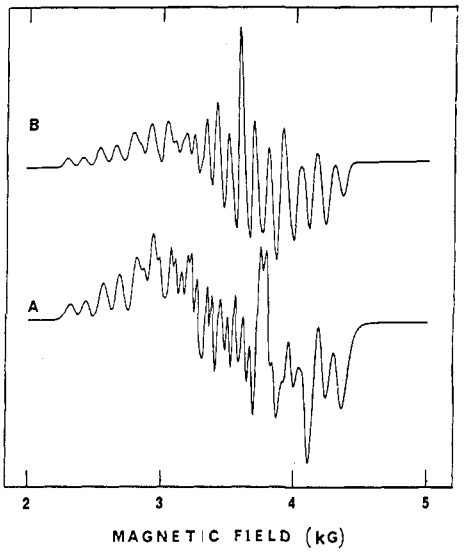

Figure 7. Experimental spectrum A and the *best* simulation B of the 7.5 K X-band EPR spectrum for an acetone/toluene/ethanol (2:1:2) frozen glass of $[Mn_2(bpmp)(\mu\text{-}OAc)_2](ClO_4)_2 \cdot H_2O$ (**1**). The simulation was carried out with an anisotropic **g** tensor as well as anisotropic **A** tensors for the Mn^{II} and Mn^{III} ions, using $g_z = 2.064$, $g_x = 1.785$, $g_y = 1.931$, line widths of $W_x = 30 \times 10^{-4}$ cm^{-1}, $W_y = 17 \times 10^{-4}$ cm^{-1}, $W_z = 30 \times 10^{-4}$ cm^{-1}, and the hyperfine parameters: A_z, $Mn^{(1)} = 250 \times 10^{-4}$ cm^{-1}, $Mn^{(2)} = 117 \times 10^{-4}$ cm^{-1}; A_x, $Mn^{(1)} = 87 \times 10^{-4}$ cm^{-1}, $Mn^{(2)} = 107 \times 10^{-4}$ cm^{-1}; A_y, $Mn^{(1)} = 130 \times 10^{-4}$ cm^{-1}, $Mn^{(2)} = 87 \times 10^{-4}$ cm^{-1}.

ground state of a valence-trapped $Mn^{II}Mn^{III}$ complex has an isotropic **g** tensor, then $(2I_1 + 1)(2I_2 + 1) = (6)(6) = 36$ manganese hyperfine lines are expected. If the **g** tensor for the $S = {}^1/_2$ ground state is axial, then a total of 72 manganese hyperfine lines are expected; a rhombic **g** tensor should lead to 108 hyperfine lines.

Attempts were made to simulate the multiline 7.5 K EPR spectra illustrated in Figure 6 with the computer program MPOW2,[20] which employs the spin Hamiltonian

$$\hat{H} = \beta\hat{S}\cdot\hat{g}\cdot\hat{H} + \hat{I}_1\cdot\hat{A}_1\cdot\hat{S} + \hat{I}_2\cdot\hat{A}_2\cdot\hat{S} \qquad (5)$$

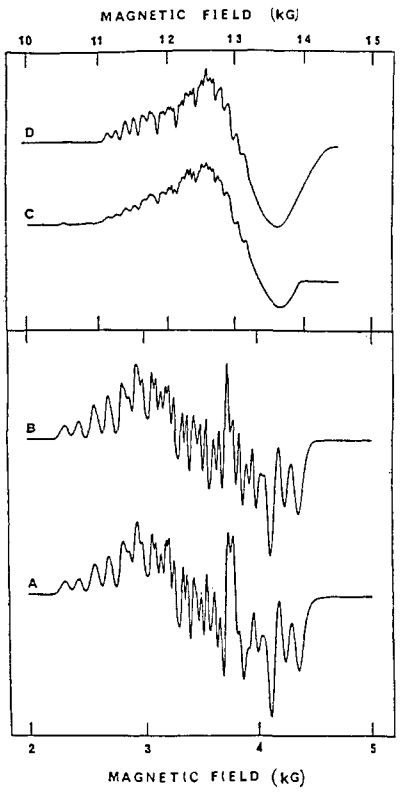

Figure 8. Simulated and observed 7.5 K X-band and ~20 K Q-band EPR spectra for an acetone/toluene/ethanol (2:1:2) glass of $[Mn_2(bpmp)(\mu\text{-}OAc)_2](ClO_4)_2 \cdot H_2O$ (**1**). Spectrum A is the observed X-band spectrum; spectrum B is the simulated X-band spectrum using $g_z = 2.026$, $g_x = 1.813$, $g_y = 1.883$, line widths of $W_x = W_y \simeq 67 \times 10^{-4}$ cm^{-1} and M_I-dependent line width $W_z = 12 + 0.9(M_I^{(1)} + M_I^{(2)})^2$ ($\times 10^{-4}$ cm^{-1}, where $M_I^{(i)}$ is the nuclear-spin quantum number on the ith Mn ion), and the hyperfine parameters A_z, $Mn^{(1)} = 267 \times 10^{-4}$ cm^{-1}, $Mn^{(2)} = 113 \times 10^{-4}$ cm^{-1}; $A_x = A_y$, $Mn^{(1)} = 145 \times 10^{-4}$ cm^{-1}, $Mn^{(2)} = 65 \times 10^{-4}$ cm^{-1}. Spectrum C is the observed Q-band spectrum; spectrum D is the simulated Q-band spectrum, using the same parameters as for the X-band spectrum except the line-width parameters $W_z = 18 + 0.9(M_I^{(1)} + M_I^{(2)})^2$ ($\times 10^{-4}$ cm^{-1}) and $W_x = W_y \simeq 100 \times 10^{-4}$ cm^{-1}. Unfortunately, the Q-band magnet operated only up to ~14 kG.

where the manganese hyperfine interaction through second order is included for two inequivalent ^{55}Mn ($I = {}^5/_2$) nuclei. Considerable time and effort were expended to find a good simulation assuming an anisotropic **g** tensor with g_x, g_y, and g_z parameters, anisotropic nuclear hyperfine interactions for both manganese centers (A_{1x}, A_{1y}, A_{1z} and A_{2x}, A_{2y}, A_{2z} parameters, and reasonable line widths for the three **g** tensor components (W_x, W_y, W_z) in the range 10×10^{-4}–30×10^{-4} cm^{-1}. Figure 7 illustrates the best simulated spectrum obtained for complex **1** by varying all of these parameters; the experimental spectrum is shown for comparison. It can be seen that only the five low-field lines and the three high-field lines in the simulated spectrum correspond well in magnetic-field position to the features seen in the experimental spectrum. However, even though the field positions are good, the relative intensities for these same lines are not comparable with those seen in the experimental spectrum. Furthermore, and even more disappointingly, the main central part of the spectrum *cannot* be simulated well even with all of these parameters. This lack of success with simulation led us to obtain additional spectra at Q-band frequency.

Q-band EPR spectra were taken for frozen glasses of complexes **1** and **2** at ~20 K. These spectra are shown in Figures 8 and 9. At the outset of these experiments it was naively anticipated that the higher frequency (~9 vs ~35 GHz) EPR experiments would separate the three components of the $S_T = {}^1/_2$ **g** tensor from each other. As can be seen from both Figures 8C and 9C the three components of the **g** tensor for the $S_T = {}^1/_2$ state which were assumed to overlap at X-band frequencies did *not* appear to separate at Q-band frequency. After detailed comparisons of the

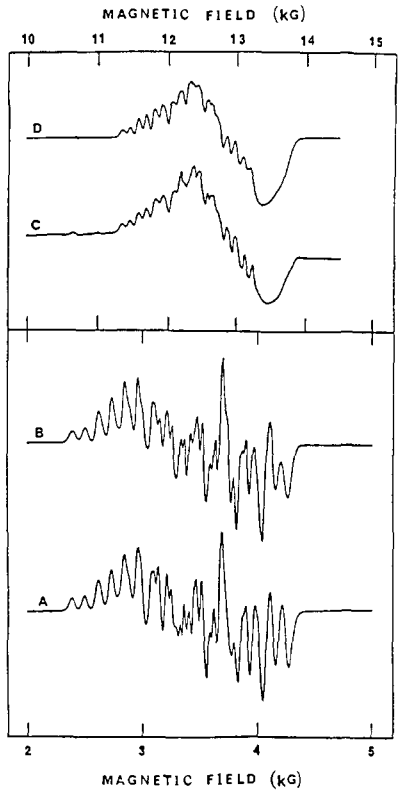

Figure 9. Simulated and observed 7.5 K X-band and ~20 K Q-band EPR spectra for an acetone/toluene/ethanol (2:1:2) glass of $[Mn_2(bcmp)(\mu\text{-}OAc)_2](ClO_4)_2 \cdot CH_2Cl_2$ (**2**). Spectrum A is the observed X-band spectrum; spectrum B is the simulated X-band spectrum using $g_z = 2.022$, $g_x = 1.905$, $g_y = 1.905$, line widths of $W_x = W_y \simeq 58 \times 10^{-4}$ cm^{-1} and M_I-dependent line width $W_z = 12.6 + 0.8(M_1^{(1)} + M_1^{(2)})^2$ ($\times 10^{-4}$ cm^{-1}), where $M_1^{(i)}$ is the nuclear-spin quantum number of the ith Mn ion, and the hyperfine parameters A_z, $Mn^{(1)} = 245 \times 10^{-4}$ cm^{-1}, $Mn^{(2)} = 106 \times 10^{-4}$ cm^{-1}; $A_x = A_y$, $Mn^{(1)} = 153 \times 10^{-4}$ cm^{-1}, $Mn^{(2)} = 73 \times 10^{-4}$ cm^{-1}. Spectrum C is the observed Q-band spectrum; spectrum D is the simulated Q-band spectrum using the same parameters as for the X-band spectrum except the line-width parameters $W_z = 20 + 0.8(M_1^{(1)} + M_1^{(2)})^2$ ($\times 10^{-4}$ cm^{-1}) and $W_x = W_y \simeq 93 \times 10^{-4}$ cm^{-1}. Unfortunately, the Q-band magnet operated only up to ~14 kG.

X- and Q-band spectra we came to the totally unexpected conclusion that only one of the **g** tensor components (g_z) is seen in either the X- or Q-band spectra and that hyperfine lines associated with the other two components (i.e., g_x, g_y) had broadened to the point of not contributing significantly to the observed EPR spectra. On the basis of this hypothesis, successful simulations of the X- and Q-band EPR spectra for both complexes could be obtained, as is shown in Figure 8 (B and D traces) for complex **1** and Figure 9 (B and D traces) for complex **2**. It must be emphasized that the same set of parameters with the exception of line widths were employed to simulate both the X- and Q-band spectra for each complex. Also, the **g** tensors and the two hyperfine tensors are assumed to be collinear, although this is not strictly required by the symmetry of the complex.

The 7.5 K X-band and 20 K Q-band spectra for complex **1** can be simulated by assuming a rhombic **g** tensor with $g_x \cong 1.813$, $g_y \cong 1.883$, and $g_z \cong 2.026$, and with axial hyperfine tensors with $A_{1z} = 267 \times 10^{-4}$ cm^{-1}, A_{1x} and $A_{1y} = 145 \times 10^{-4}$ cm^{-1}, and $A_{2z} = 113 \times 10^{-4}$ cm^{-1} and A_{2x} and $A_{2y} = 65 \times 10^{-4}$ cm^{-1}. Line widths were taken as $W_x = W_y \cong 67 \times 10^{-4}$ cm^{-1} and W_z (10^{-4} cm^{-1}) $= 12 + 0.9(M_1^{(1)} + M_1^{(2)})^2$ for the X-band spectrum and $W_x = W_y \cong 100 \times 10^{-4}$ cm^{-1} and W_z (10^{-4} cm^{-1}) $= 18 + 0.9(M_1^{(1)} + M_1^{(2)})^2$ for the Q-band spectrum, where $M_1^{(i)}$ is the nuclear-spin quantum number for the ith manganese nucleus. The spectra for complex **2** can be simulated assuming an axial **g** tensor for the $S = {}^1/_2$ state. The simulation parameters are $g_x = g_y \cong 1.905$ and $g_z = 2.022$ with axial hyperfine tensors where $A_{1z} = 245 \times 10^{-4}$ cm^{-1}, $A_{1x} = A_{1y} = 153 \times 10^{-4}$ cm^{-1}, $A_{2z} = 106 \times 10^{-4}$ cm^{-1}, and $A_{2x} = A_{2y} = 73 \times 10^{-4}$ cm^{-1}. For complex **2** the line widths were taken as $W_x = W_y \cong 58 \times 10^{-4}$ cm^{-1} and $W_z = 12.6 + 0.8(M_1^{(1)} + M_1^{(2)})^2$ (10^{-4} cm^{-1}) for the X-band spectrum and $W_x = W_y \cong 93 \times 10^{-4}$ cm^{-1} and $W_z = 20 + 0.8(M_1^{(1)} + M_1^{(2)})^2$ (10^{-4} cm^{-1}) for the Q-band spectrum. In Figures 8 and 9 it can be seen that these simulated spectra compare very favorably with the experimental spectra.

For exchange-coupled ions in which the exchange interaction is much larger than the Zeeman and hyperfine interactions, the spin operators of the component ions are added *vectorially* to give the total spin operator; the component spins are said to be quantized along the total spin. We may therefore express the magnetic parameters of the cluster (effective g and A values) in terms of the values for the isolated ions. In terms of the projection along each spin these relationships are $A_1 = A'_1(S_1 \cdot S/S^2)$ and $A_2 = A'_2(S_2 \cdot S/S^2)$, where A_1 and A_2 are hyperfine constants for the cluster and A'_1 and A'_2 are those for the isolated ions. The projections have been evaluated for the high-spin case $S_1 = {}^5/_2$, $S_2 = 2$, and $S = {}^1/_2$, where the equations become $A_1 = {}^7/_3 A'_1$ and $A_2 = -{}^4/_3 A'_2$, assuming that the larger hyperfine coupling is due to Mn^{II} and the smaller is due to Mn^{III}. Using the parameters obtained from the simulation, we can calculate the isotropic hyperfine coupling constants for the cluster, assuming that A_x, A_y, and A_z have the same sign. Using the values of 186×10^{-4} and 81×10^{-4} cm^{-1} for complex **1**, we obtain $A'_1 = 80 \times 10^{-4}$ cm^{-1} for Mn^{II} and $A'_2 = 61 \times 10^{-4}$ cm^{-1} for Mn^{III}. Similarly for complex **2**, which has isotropic coupling constants of 184×10^{-4} cm^{-1} and 84×10^{-4} cm^{-1}, we find $A'_1 = 79 \times 10^{-4}$ cm^{-1} for Mn^{II} and $A'_2 = 63 \times 10^{-4}$ cm^{-1} for Mn^{III}. The large differences between the hyperfine constants for Mn^{II} vs Mn^{III} indicate that the unpaired electron in the $S = {}^1/_2$ ground state is localized on one of the Mn ions or transferred between them at a rate much slower than ($||A_1| - |A_2||$). In isolated ions the hyperfine field per electron is expected to be nearly constant based on the spin polarization of the core electrons by the outer d electrons. Accordingly, the hyperfine field for Mn^{II}, Mn^{III}, and Mn^{IV} should all be about the same magnitude and sign (negative) except reduced somewhat for the higher oxidation states owing to an increased effect of covalency. Table VI gives the hyperfine constants (A_x, A_y, A_z) seen for various oxidation levels of manganese ions having 6-fold coordination to oxygen in different host crystals.[40-47a] From this table, the isotropic hyperfine coupling constants are found to be of the same order of magnitude, except for a slight decrease with increasing oxidation state. Thus, for Mn^{II} $A \cong -80 \times 10^{-4}$ cm^{-1} and for Mn^{III} and Mn^{IV} $A \cong -70 \times 10^{-4}$ cm^{-1}. It should also be noted that the hyperfine field will also decrease as the ratio of the covalency of the Mn ligand to the coordination number increases as reported in detail for Mn^{II}.[47b] Our values calculated for the isolated Mn^{II} ion of 80×10^{-4} cm^{-1} for complex **1** and 79×10^{-4} cm^{-1} for complex **2** are in the range expected for six-coordinate Mn^{II} in a weak ligand field. The A'_2 values of 61×10^{-4} cm^{-1} and 63×10^{-4} cm^{-1} for complexes **1** and **2**, respectively, are somewhat lower than expected for six-coordinate Mn^{III} in a weak ligand field. The sign of A'_1 and A'_2 should be both negative as expected for isolated Mn^{II} and Mn^{III} ions, which means that A_1 and A_2 should have opposite signs (A_1 negative, A_2 positive).

The highly anisotropic line broadening observed in this study, wherein the g_z hyperfine features are much narrower than the g_x and g_y hyperfine features, could have several different origins. If nitrogen superhyperfine structure is not resolved in the EPR spectrum of a nitrogen-ligation complex, then there is a large increase in the residual line width. This has been investigated by studying a number of oxygen-ligation and/or nitrogen-ligation copper(II) complexes.[48] Oxygen ligation copper complexes, e.g., $[Cu(H_2O)_6]^{2+}$ and [Cu(catechol)$(H_2O)_4$], have narrower residual

(42) Gerritsen, H. J.; Sabisky, E. S. *Phys. Rev.* **1963**, *132*, 1507.
(43) Andresen, H. G. *Phys. Rev.* **1960**, *120*, 1606.
(44) Low, W.; Suss, J. T. *Phys. Rev.* **1961**, *119*, 132.
(45) Lavrance, N.; Lambe, V. *Phys. Rev.* **1963**, *132*, 1029.
(46) Davies, J. J.; Smith, S. R. P.; Wertz, J. E. *Phys. Rev.* **1969**, *178*, 608.
(47) (a) Oyen, G. L.; Woonton, G. A. *Can. J. Phys.* **1967**, *45*, 2975. (b) Simonek, E.; Muller, K. A. *J. Phys. Chem. Solids* **1970**, *31*, 1027.
(48) Froncisz, W.; Hyde, J. S. *J. Chem. Phys.* **1980**, *73*, 3123.

line widths associated with hyperfine structure in the $g_{\parallel}$ region than does the Cu^{II} complex of the amino acid DOPA (3,4-dihydroxyphenylalanine), where no resolved nitrogen superhyperfine could be observed. In the present work, complexes **1** and **2** have elongated Mn^{III}–N bonds in the z direction, and as such the manganese hyperfine structure on the x and y components of the **g** tensor could have more unresolved nitrogen superhyperfine, which would increase the residual line widths of hyperfine structure on the x and y **g** tensor components. This could explain in part why only hyperfine structure associated with the z component of the **g** tensor is seen.

Another source of line width is "g strain" and/or "A strain". A theory[48] has been developed that describes the line widths of the parallel region (i.e., $g_{\parallel}$ hyperfine features) of spectra for Cu^{II} complexes in terms of four parameters: (i) the residual line width, σ_R; (ii) the distribution of hyperfine values $A_{\parallel}$ arising from strain, σ_A; (iii) the distribution of $g_{\parallel}$ values arising from strain, σ_g; (iv) the degree of correlation of these two distributions, σ_{Ag}. The phenomenon of "g strain" results from a distribution of different molecular environments as would be found in a glass. If there is a Gaussian distribution of g values (with a half-width of Δg) about the mean value (which could be the measured g value), this produces a corresponding line width (σ_g), which is given as $\sigma_g = (\Delta g/g)\nu_0$, where ν_0 is the microwave frequency.

A distribution of molecular environments in a frozen glass may also lead to a distribution of manganese hyperfine values. The line broadening from "g–A strain" depends on the microwave frequency and on the magnitude of the nuclear hyperfine interaction for both metal ions in a binuclear complex. To understand thoroughly the mechanism of line broadening seen for the hyperfine structure on the x and y components of the $S = {}^1/_2$ **g** tensor, it is necessary to have a systematic study of line widths taken at several different frequencies in the EPR experiment.

In summary, the manganese hyperfine structure observed in the $g \cong 2$ signal of the 7.5 K frozen-glass EPR spectra of complexes **1** and **2** arises predominantly from manganese hyperfine on the z component of the **g** tensor for the $S = {}^1/_2$ ground state. The manganese hyperfine lines on the x and y components are broadened to the point that they contribute only to the background of the $g \cong 2$ signal in the X- and Q-band spectra. Strain effects associated with distributions of molecular environments in the frozen glass could be the origin of these effects. It is important to emphasize that many variations of all the parameters were tried in simulating the hyperfine patterns shown in Figures 8 and 9. Figure 10 illustrates several other simulated X-band spectra for complex **1** to underscore the fact that there is no other obvious way to simulate the experimental spectra. For all of the simulations shown in Figure 10 the same G, A_1 and A_2 values are used as were used in the simulations for the spectra of complex **1** shown in Figure 8. As can be seen in Figure 10 (simulation a) relatively narrow line widths for the hyperfine structure on all three components give too many lines, more than 35 lines compared to the experimental spectrum, which shows 29 lines. There is also too much intensity in the high-field region. Simulation b of Figure 10 shows that increasing the hyperfine structure in the z component of the **g** tensor leads to a loss of low-field hyperfine features, whereas an increase in the line width of the x-component features (simulation c) leads to too much intensity in the midfield range. Broadening the line width of hyperfine structure on the g_y component (simulation d) also does not lead to a good simulation of the experimental spectrum in Figure 10. Finally, in simulation e the effect of increasing the line width of hyperfine structure on all three **g**-tensor components leads to a poorly resolved simulated spectrum. The inescapable fact is that the manganese hyperfine structure on the g_x and g_y signals is quite broad compared to that on the g_z signal in the 7.5 K glass spectra of complexes **1** and **2**.

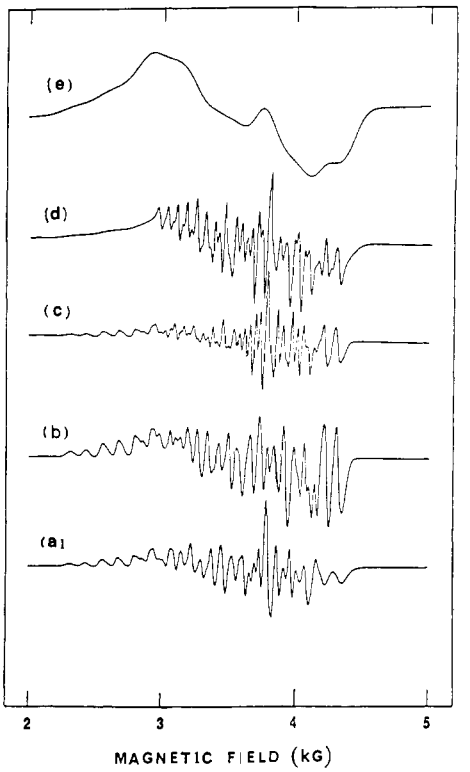

Figure 10. Simulated X-band spectra with different line-width parameters for $[Mn_2(bpmp)(\mu\text{-}OAc)_2](ClO_4)_2\cdot H_2O$ (**1**). All of these simulations were carried out using the same g, A_1, and A_2 values as employed for the X-band simulation shown in Figure 8. The various line widths employed are as follows, with values for spectra a–e given in the order W_x ($\times 10^{-4}$ cm^{-1}), W_y ($\times 10^{-4}$ cm^{-1}), W_0 ($\times 10^{-4}$ cm^{-1}): (a) 12, 12, 12; (b) 12, 12, 67; (c) 67, 12, 12; (d) 12, 67, 12; (e) 67, 67, 67; where $W_z = W_0 + 0.9(M_1^{(1)} + M_1^{(2)})^2$ ($\times 10^{-4}$ cm^{-1}).

Concluding Comments

The preparation and X-ray structures have been reported for two valence-trapped $Mn^{II}Mn^{III}$ complexes, $[Mn_2(bpmp)(\mu\text{-}OAc)_2](ClO_4)_2\cdot H_2O$ (**1**) and $[Mn_2(bcmp)(\mu\text{-}OAc)_2](ClO_4)_2\cdot CH_2Cl_2$ (**2**). Each of these complexes shows two quasi-reversible one-electron waves, one corresponding to a reduction to the Mn^{II}_2 complex and the other to an oxidation to the Mn^{III}_2 complex. Weak magnetic exchange interactions were found for both complexes with exchange parameters of $J = -6.0$ and -7.7 cm^{-1} for complexes **1** and **2**, respectively. The main emphasis of this paper has been on the interpretation of the manganese hyperfine-structured $g \cong 2$ EPR signal seen for **1** and **2** in a glass at liquid-helium temperatures. By careful simulation of X- and Q-band data, it is shown that the 29-line hyperfine patterns seen at X-band frequency in the 7.5 K glass spectra are dominated by only manganese hyperfine structure on the z component of the **g** tensor. Strains in **g**, **A**, or **D** tensors, resulting from distributions in molecular environments in the glass, likely lead to hyperfine lines on the x and y components of the ground-state **g** tensor that are so broad that they are hardly seen.

If the S_2 state of PS II has a $Mn^{IV}Mn^{III}_3$ site, then the S_0 state, which is two electrons reduced from the S_2 state, would have a $Mn^{II}Mn^{III}_3$ description. In view of the present results it is perhaps understandable why no EPR signal has been reported for the S_0 state. It is clear that the magnetic exchange interaction in a Mn^{II}–B–Mn^{III} pair that is bridged by some combination of phenoxide, halide, or carboxylate moieties is quite weak. This leads to low-lying excited states in a binuclear $Mn^{II}Mn^{III}$ complex or even a tetranuclear $Mn^{II}Mn^{III}_3$ complex. Not only will **g**, **A**, or **D** strain effects also be likely to broaden some parts of the EPR signal for a complex containing a $Mn^{II}Mn^{III}$ unit, but low-lying excited states will lead to the Orbach spin–lattice relaxation process.[49] Spin–lattice relaxation times for a $Fe^{II}(\S)Fe^{III}$ protein site were deduced from line widths measured by spectral simulation and the observed temperature dependencies were interpreted in terms of an Orbach mechanism in a study by Gayda et al.[50]

(49) Orton, J. W. *Electron Paramagnetic Resonance*; Gordon and Breach: New York, 1968.

(50) Gayda, J.-P.; Gibson, J. F.; Cammack, R.; Hall, D. O.; Mullinger, R. *Biochim. Biophys. Acta* **1976**, *434*, 154.

The EPR signal for the S_2 state of PS II is really a difference spectrum between those for PS II in the S_2 state and PS II in the S_1 state.[7,8] Such S_2-state EPR spectra were determined at different frequencies by Hansson et al.[51] They found that the 18-20 manganese hyperfine lines on the $g \cong 2$ signal observed at 9.4 GHz did not separate into identifiable hyperfine-structured g_x, g_y, or g_z signals at 36 GHz. It could be concluded that the **g**-tensor anisotropy is too small to be seen at 34 GHz. Alternatively, it is possible that at both X- and Q-band frequencies the manganese hyperfine structure on only one of the **g**-tensor components of the $S = {}^1/_2$ state is seen. Distributions in environments about the polymanganese S_2 state in the chloroplast could lead to strain effects.

Several $Mn^{III}Mn^{IV}$ complexes such as $[(bipy)_2Mn<^{O}_{O}>Mn(bipy)_2]^{3+}$ have been shown[32-34] to give in a glass medium $g \cong 2$ EPR signals which are structured with 16 manganese hyperfine lines. These $Mn^{III}Mn^{IV}$ complexes exhibit antiferromagnetic interactions with exchange parameters in the range $J = -40$ to -220 cm^{-1}. All simulations of these spectra have been performed by assuming an isotropic **g** tensor for the $S = {}^1/_2$ ground state, together with isotropic hyperfine **A** tensors for the Mn^{III} and Mn^{IV} ions. Very recently, the EPR spectrum reported[32b] for a *polycrystalline* sample of a $Mn^{III}Mn^{IV}$ complexes was also found to exhibit a 16-line manganese hyperfine pattern. Careful examination of the simulated and experimental EPR spectra for these $Mn^{III}Mn^{IV}$ complexes shows that the simulations are not very good. Only some signals at low field and at high field are simulated well. However, the relative intensities and line shapes are in many cases quite different between the simulated and experimental spectra. This is particularly true for the hyperfine-structured $g \cong 2$ signal seen[32b] for the polycrystalline sample of $[L_2Mn_2(\mu\text{-}O)_2(\mu\text{-}O_2CCH_3)](BPh_4)_2 \cdot CH_3CN$, where L is 1,4,7-triazacyclononane. There are no Q-band EPR spectra presented for these $Mn^{III}Mn^{IV}$ complexes. To see if the EPR spectra for $Mn^{III}Mn^{IV}$ complexes have the same broadening effects as seen in the spectra of **1** and **2**, it is important to try other EPR frequencies for the experiments.

Finally, it is quite relevant to note that Khangulov et al.[52] and Fronko et al.[53] have recently reported a variety of EPR signals for the T-catalase from Thermus thermophilus, an enzyme that the 3-Å-resolution X-ray structure[54] shows to have a binuclear Mn site. Treatment of samples of the enzyme with either different exogenous ligands or oxidants or by variation in the temperature gives superpositions of a variety of manganese multiline hyperfine-structured EPR signals. These signals have been attributed to enzymes with either Mn^{II}_2, $Mn^{II}Mn^{III}$, or $Mn^{III}Mn^{IV}$ binuclear sites. Some of these EPR signals do bear some resemblance to those reported in this paper for complexes **1** and **2**.

Acknowledgment. We are grateful for support from NIH Grants HL 13652 (D.N.H.), 1510 RRO 148601A1 (crystallographic instrumentation at Rutgers, H.J.S.), and the Rutgers research council (S.S.I.).

Supplementary Material Available: Tables of experimental and calculated magnetic susceptibility data for complexes **1** and **2**, figure showing fit of data for complex **2**, tables of atomic coordinates and equivalent isotropic thermal parameters for complexes **1** and **2**, tables of H atom parameters and anisotropic thermal parameters for complexes **1** and **2**, and figures showing electrochemistry, 400 MHz ^{1}H NMR, and X-band EPR data for complexes **1** and **2** (22 pages); tables of observed and calculated structure factors for **1** and **2** (66 pages). Ordering information is given on any current masthead page.

(51) Hansson, O.; Aasa, R.; Vanngard, T. *Biophys. J.* **1987**, *51*, 825.

(52) Khangulov, S. V.; Barynin, V. V.; Melik-Adamyan, V. R.; Grebenko, A. I.; Voevodskaya, N. V.; Blumenfeld, L. A.; Dobryakov, S. N.; Il Yasova, B. V. *Bioorg. Khim.* **1986**, *12*, 741-748.

(53) Fronko, R. M.; Penner-Hahn, J. E.; Bender, C. J. *J. Am. Chem. Soc.* **1988**, *110*, 7554-7555.

(54) Barynin, V. V.; Vagin, A. A.; Melik-Adamyuan, V. R.; Grebenko, A. I.; Khangulov, S. V.; Popov, A. N.; Andrianova, M. E.; Vainshtein, B. K. *Sov. Phys. Dokl.* **1986**, *31*, 457-459.

Differential Line Broadening in the NMR Spectrum of Methanol Adsorbed on Sol–Gel Silica

C. J. Hartzell, P. C. Stein, T. J. Lynch,[†] L. G. Werbelow,*[,‡] and William L. Earl*

Contribution from the Los Alamos National Laboratory, Los Alamos, New Mexico 87545.
Received October 3, 1988

Abstract: The nuclear magnetic relaxation characteristics of (^{13}C)methanol adsorbed to sol-gel silica were studied over a wide range of temperatures. The four-line spectra displayed different T_2 values for each line. Inner and outer lines of the quartet displayed different T_1 values. This behavior indicates that temporal correlations between different carbon-proton dipolar interactions are significant. Cross correlations between carbon-proton dipolar couplings and the carbon chemical shift anisotropy are discernible. Adsorbed methanol presents an interesting situation where both even and odd ranks of multispin order are spawned from athermal magnetizations via orientationally dependent spin interactions. These interactions are modulated by highly anisotropic molecular motions.

Various NMR relaxation methodologies provide the chemical researcher with sensitive probes of dynamical structure at the molecular level. Although molecular motions result in the averaging of anisotropic spin couplings, both the nature of the motional averaging process and the magnitude of the anisotropy can be revealed through analysis of the NMR relaxation experiment. Of interest in this work are NMR relaxation studies that probe the creation and subsequent dissipation of multispin order. Temporal correlations between competing orientationally dependent spin interactions generate multispin order in a manner analogous to the generation of multispin order in popularized variants of multipulse NMR.

Although the foundations of multispin NMR relaxation spectroscopy were developed many years ago and are couched in a convenient product operator formalism,[1] only recently has in-

[†] Department of Chemistry, University of Nevada, Reno, NV 89557.
[‡] Department of Chemistry, NMIMT, Socorro, NM 87801.

0002-7863/89/1511-5114$01.50/0